

**A BRAIN MODEL FOR THE STUDY OF
MR SUSCEPTIBILITY INDUCED PHASE BEHAVIOR**

A BRAIN MODEL FOR THE STUDY OF
MR SUSCEPTIBILITY INDUCED PHASE BEHAVIOR

BY

SAGAR BUCH

A Thesis

Submitted to the School of Graduate Studies

in Partial Fulfillment of the Requirements

for the Degree of

M.A.Sc.

(Master of Applied Science)

in Biomedical Engineering

McMaster University

© Copyright by Sagar Buch, July 2012

M.A.Sc. (2012)

McMaster University

(Biomedical Engineering)

Hamilton, ON, Canada

TITLE: A Brain Model for the Study of MR Susceptibility Induced Phase
Behavior

AUTHOR: Sagar Buch (McMaster University)

SUPERVISOR: Professor E. Mark Haacke

NUMBER OF PAGES: xii, 97

Abstract:

MR phase images contain essential information about local magnetic susceptibility sources in the brain. Appropriately processed, the phase images can be used to reconstruct these susceptibility sources creating a new type of contrast in magnetic resonance imaging (MRI). The goal of this thesis is to demonstrate with a model of the brain how accurately the transformation of phase to susceptibility takes place.

A 3D brain model uses the Forward process to calculate magnetic field perturbations caused by susceptibility properties of the tissues in the model. Homodyne High Pass (HP) filter and SHARP algorithm, two methods commonly used to remove background field variations, are used to process the simulated phase images. Similarly, MR Gradient echo magnitude data are simulated by defining the structures of the model with tissue properties such as T_1 , T_2^* relaxation times and spin density.

Introducing simulated phase with image imperfections, such as partial volume due to discretization of the acquired signal and addition of white Gaussian noise, shows good agreement with the real phase data. Susceptibility mapping using inverse process is analyzed to understand the error in reconstructing the actual susceptibility distribution.

The brain model demonstrates how the Iterative algorithm corrects the ‘streaking’ artifact introduced by the singularity region in k-space during the inverse process. T_2^* maps are produced from multiple echo simulations to identify the changes in actual T_2^* values due to microstructural magnetic field variations especially at the edges of structures like veins or globus pallidus.

The halo ring around red nucleus in the real phase data is believed to be an indicator of a capsule around red nucleus. Similar effect is seen in the simulated phase images without including the capsule of red nucleus in the brain model, this comparison explains that the halo effect may just be entirely or a part of the phase behavior around red nucleus. A negative susceptibility in the internal capsule region, seen in both simulated and real susceptibility maps, is discussed as a possible artifact caused by the processing techniques after comparing the simulated susceptibility maps produced from unprocessed and processed phase data. The brain model is used to determine the optimum echo time of the initial gradient echo sequence in order to produce a high quality susceptibility map with reasonably low error and better time efficiency. The results of simulating the effects of different echo times suggest a range of 13 to 16 ms as being optimal.

Acknowledgements

I would like to sincerely thank my supervisor, Dr. E. Mark Haacke, for all his guidance and support throughout my study at McMaster University. Dr. Haacke and his works have been and will always be a huge source inspiration for me. Even in his busy schedule, he always has time for his students to sort out their problem and, almost always, give them new ideas to think about. It has been an unbelievable privilege to work under his guidance.

I am very thankful to Dr. Michael Noseworthy for providing us students with immensely helpful courses in medical imaging. His light-hearted, yet very informative, approach of teaching the students is very admirable and attending his classes has always been a delight.

I would also like to acknowledge Dr. Yu-Chung Norman Cheng and Dr. Jaladhar Neelavalli at Wayne State University, for their help and time they spent in clearing my doubts. I wish to thank my colleagues at McMaster, Jin Tang, Saifeng Liu and Karen Mok, for sharing their knowledge and experiences that has been instrumental in my research work.

I wish to thank my parents, my mother, Bharati Buch and my father, Dr. Yatrik Buch, for the immense love and support they gave me throughout my life. I could not have come so far without them. This thesis is dedicated to them.

Table of contents:

Chapter 1: Introduction 1

Chapter 2: Basics of MRI Phase Signal 7

 2.1 MRI Signal 7

 2.2 Magnetic Susceptibility 9

 2.3 Gradient Echo Imaging 13

 2.4 SWI Pulse Sequence 15

 2.5 Complex MR Signal 17

 2.6 Phase Aliasing 18

 2.7 Magnetic Field Perturbations ($\Delta B(\vec{r})$) 20

 2.8 Filtered-Phase Images (Homodyne High Pass filter) 24

 2.9 Forward Method for Calculating Magnetic Field Perturbations..... 26

 2.10 Susceptibility Mapping using Inverse Process 29

Chapter 3: Three Dimensional model of the brain 35

 3.1 Structures of the Brain Model..... 36

 3.1.1 Basal Ganglia..... 37

 3.1.2 White Matter and Grey Matter..... 40

 3.1.3 Cerebellum..... 43

 3.1.4 Venous Network..... 44

 3.2 Validation of the Extracted Geometries..... 45

 3.3 Applications of the Brain Model..... 50

 3.3.1 Analysis of Phase Processing Techniques..... 51

 3.3.2 Comparison with Real Phase Data..... 59

Chapter 4: T_2^* mapping Using the Simulated Brain Model 77

 4.1 Basics of MRI Magnitude Signal..... 77

 4.2 T_2^* Mapping..... 81

 4.3 T_2^* Mapping Using the Brain Model..... 84

 4.4 T_2^* Error and Signal Loss..... 86

Chapter 5: Future Directions..... 95

List of Figures:**Chapter 2:**

Figure 2.1: *The precession of a spin after the application of an RF pulse, a), which generates free induction decay (FID) signal, b).* 9

Figure 2.2: *Basics of a Gradient echo sequence. a) The effects of applying a positive or negative gradient field in presence of the main external magnetic field (B_0), b) A simple representation of a Gradient Echo pulse sequence.* 14

Figure 2.3: *Pulse sequence diagram for 3D gradient echo MR acquisition with flow compensation in all three directions to reduce the effects of pulsatility effects of the blood or cerebrospinal fluid flow. The pulse sequence includes first order gradient moment nulling in readout (G_r) and slice-select (G_s) directions. The partition encoding and phase encoding (G_p) gradients are velocity compensated with respect to the echo.* 17

Figure 2.4: *Complex representation of an MR signal acquired through ‘Real’ and ‘Imaginary’ channels. $|S|$ represents the magnitude and φ is the phase component of an MR signal.* 19

Figure 2.5: *A cylinder with a radius ‘a’ placed at an angle θ to the external magnetic field B_0 and is the polar angle in the x-y plane of the point ‘p’ relative to the external field. The magnetic field variation outside the cylinder at a point ‘p’ with a distance ρ can be defined by Equation 2.17.* 23

Figure 2.6: *a) Original unfiltered phase image with imaging parameters: $TE=20ms$, $B_0=3Tesla$ with $0.5 \times 0.5 \times 2mm^3$ resolution and b) Homodyne high pass filtered phase image with filter size of 64×64 pixels, which shows the underlying tissue information much clearly by reducing the background field variations.* 25

Figure 2.7: *a) Original susceptibility map (SM) of a 3D brain model (Chapter 3), b) Simulated phase generated by using the Forward calculation of field perturbations*

(Please refer to Equation 2.27) at $TE=20ms$ and $B_0=3Tesla$, c) SM reconstructed from phase information in b) using the Inverse process (Please refer to Equation 2.28). 29

Chapter 3:

Figure 3.1: a) Susceptibility map of the real data with imaging parameters: $TE=20ms$ and Main field strength= $3Tesla$, b) Simulated susceptibility map produced by extracting the basal ganglia structures. CN=Caudate Nucleus, PUT=Putamen, GP=Globus Pallidus, TH=Thalamus. Please refer to **Figure 3.11** for the structures in mid-brain.

38

Figure 3.2: Segmentation of grey matter (GM), white matter (WM) and cerebrospinal fluid (CSF) using Double Inversion Recovery (DIR) sequences. DIR_1 ($TE=1.46ms$, $TR=3100ms$, $3T$) suppresses WM signal whereas DIR_2 ($TE=1.57ms$, $TR=2800ms$, $3T$) suppresses signals of GM and CSF. The image c) shows the brain model with the segmented GM, WM and CSF tissues.

43

Figure 3.3: Validation of the extracted structures using Human Subcortical Atlas made by Johns Hopkins University (JHU). a) Caudate nucleus, b) Putamen, c) Globus pallidus, d) Thalamus. The white region in the left-half of each structure shows the overlap region between the extracted structure for the brain model and the JHU atlas. The right-half of the figures represents the extraction of the structures for the model and is given for your reference. These images are generated by volume rendering using the Volview3.4 © software, Kitware Inc. Please note that the variations seen at the edges are due to the smoothed profile at the edge of the atlas structures. The model consists of homogeneous susceptibility distribution inside the structures without any rough boundary that could create false dipole effects.

46

Figure 3.4: Transverse, Coronal and Sagittal views of the three-dimensional brain model. The structures are differentiated by their susceptibility values which are listed in

the table below the image. CN=Caudate nucleus, SN=Substantia nigra, RN=Red nucleus, GP=Globus pallidus, CC=Crus Cerebri, PUT=Putamen, TH=Thalamus, WM=White matter, GM=Grey matter, CSF=Cerebrospinal fluid, and veins. 49

Figure 3.5: Comparison of MRI real phase information processing techniques using a 3D brain model. a) Original phase image (imaging parameters $TE=18ms$ and $B_0=3T$), b) Homodyne High pass filtered phase image (filter size 64×64 pixels), c) SHARP processed phase image. Graph d) shows the profile plot of the phase distribution across the lenticular nucleus (putamen and globus pallidus) along the white-bar in a), b) and c).

53

Figure 3.6: Relationship between the mean susceptibility value inside a given structure and the processing filters used on the original phase images produced from the brain model. CN=Caudate nucleus, GP=Globus pallidus, RN=Red nucleus, PUT=Putamen, and TH=Thalamus. Imaging parameters: $B_0=3Tesla$, Echo time= $18ms$, pixel resolution= $0.5 \times 0.5 \times 0.5mm$ and regularization threshold of inverse filter= 0.1 . 54

Figure 3.7: Susceptibility maps generated from unfiltered simulated phase images (imaging parameters: $B_0=3T$, $TE=18msec$). Sagittal plane and coronal plane images shows the streaking artifacts (identified by the white arrows) introduced by the singularity problem in k -space in the inverse process. 56

Figure 3.8: Susceptibility maps before and after the iterative method using a binary mask which consists of vessels. a) Original susceptibility map without any noise added to the original simulated images (imaging parameters $TE=18ms$ and $B_0=3T$) in sagittal view, b) Iterative result of a) after three iterations, c) The difference map of a) and b), d) Same original susceptibility map as a) in coronal view, e) Iterative result of a) after three iterations in coronal view, f) The difference map of d) and e). White arrows indicate the streaking artifacts seen in the original susceptibility maps a) and d). The difference maps show that this streaking noise is almost completely removed after three iterations of iterative method. 58

Figure 3.9: *Mean susceptibility value measurements of the straight sinus a) and septal veins b), from the susceptibility maps, generated from filtered and unfiltered phase, before and after simulating the partial volume effects (mimicking the discrete sampling of the MR signal). The susceptibility value of the septal vein is more affected by the partial volume effect. The resolution of the image is $0.5 \times 0.5 \times 0.5 \text{mm}^3$ with aspect ratio of 1:1:1. The diameter of the straight sinus is around 8 pixels (4mm) and the diameter of the septal vein is 2 pixels (1mm) wide in the original model. The initial susceptibility value used inside the veins, $\Delta\chi=0.45\text{ppm}$. The partial voluming of the phase behavior around a small vessel like the septal vein severely affects the results of its reconstructed susceptibility distribution.* 61

Figure 3.10: *Comparison of a real phase data with the simulated phase with the same parameters as the real data. a) A real phase image, (Wayne State Research Facility) acquired using 3D GRE flow compensated-high resolution-SWI sequence, which is processed using SHARP (Sophisticated Harmonic Artifact Reduction on Phase data) method with imaging parameters $B_0=3\text{T}$ and $TE=18\text{ms}$. The imaging parameters and processing techniques are kept consistent in the simulated phase image b), c) A transverse view of the 3D brain model. Images a) and b) have the same window level settings.* 63

Figure 3.11: *Comparison of the real phase information with simulated model phase profile of the rostral mid-brain area. a) Rostral mid-brain area in the brain model for reference, b) Homodyne HP-filtered real phase image ($TE=20\text{msec}$, 3T , $0.5 \times 0.5 \times 2\text{mm}$ resolution, filter size 64×64 pixels), c) Homodyne HP-filtered simulated phase data (same parameters and resolution as (b)), d) SHARP processed real phase data ($TE=18\text{msec}$, 3T , $(0.5\text{mm})^3$) e) SHARP processed simulated phase data (same parameters as (d)). RN=Red Nucleus, SN=Substantia Nigra, CC=Crus Cerebri. The white arrows indicate the halo ring at the boundary of red nucleus in real and simulated phase data.* 65

Figure 3.12: *Comparison of susceptibility maps of the modeled data with various processing techniques and real data. Images show a part of basal ganglia surrounded by*

white matter, grey matter and CSF. Imaging parameters: $B_0=3T$, $TE=20msecs$ and resolution $0.5 \times 0.5 \times 2mm$. a) Susceptibility map of real data (HP filter size 64×64), b) Susceptibility map of modeled data (HP filter size 64×64), c) Susceptibility map of modeled data (unfiltered phase), d) Susceptibility map of SHARP processed phase, e), f) and g) are iterative results of (b), (c) and (d). The phase images for reconstructing the susceptibility maps shown in images b) – g) are generated using the same parameters and resolution as a). 68

Figure 3.13: a) Edge profile of susceptibility distribution from globus pallidus to the crus posterius [along the grey bar shown in Figure 3.12(b), (c), (d)]. b) Plot of mean susceptibility value over the internal capsule region (refer to the contour in Figure 3.12e)) at different HP filter sizes [actual $\Delta\chi_{(internal\ capsule)} = 0ppm$]. 69

Figure 3.14: Relationship between the echo time and the error in the susceptibility quantification in susceptibility maps. A constant white Gaussian noise (mean/standard deviation= $10/1$) was added to the real and imaginary components of the simulated data. a) The measurements are done in a homogeneous white matter region where the expected mean value is ideally zero, b) The measurements of mean χ value and the standard deviation are done inside the Globus pallidus ($\chi_{(globus\ pallidus)} = 0.18ppm$). 71

Chapter 4:

Figure 4.1: a) Recovery of the longitudinal component of the magnetization from initial value $M_z(0)$ to the equilibrium magnetization M_0 , b) The decay of the transverse magnetization from the initial value of $M_{xy}(0)$. 79

Figure 4.2: Relationship between the logarithm of the magnitude signal and the echo time (TE). A homogeneous white matter region signal from the simulated magnitude images (Figure 4.3) at different echo times (in msec: 4, 7, 10, 13, 16, 19, 22, 25) is used to plot this relationship. 84

Figure 4.3: Spin density (ρ_0), T_1 and T_2^* properties are added to each tissue in the brain model in order to generate magnitude images at main magnetic field, B_0 , of 3Tesla for different echo times ($T_n=4\text{msec}$, 7msec , 10msec , 13msec , 16msec , 19msec , 22msec and 25msec) using 4.5 where flip angle of 15° is used. The reasonable values for ρ_0 , T_1 and T_2^* tissue properties are selected from real data processing (for spin density and T_2^* values of basal ganglia structures) and literature [1, 14-21] at $TR=35\text{msec}$. 86

Figure 4.4: a) T_2^* map generated by collapsing high resolution complex data, b) T_2^* map generated by collapsing high resolution magnitude (no phase information), c) ' T_2^* residual error map' or the difference image of b) subtracted from a) represents the change in T_2^* value which is caused by the signal loss due to local field variations in a). 87

Figure 4.5: a) Zoomed image (Fourier type zooming factor) of a T_2^* map generated by collapsing complex data, b) Zoomed image of a T_2^* map generated by collapsing magnitude (no phase information), c) T_2^* 'residual error maps' are produced by subtracting b) from a). The white arrows in the error map c) clearly shows the underestimation of the actual T_2^* values at the boundary of the vessels where there is relatively high susceptibility variations. a), b) and c) are at the same slice level. 88

Figure 4.6: Comparison of the T_2^* maps, in rostral mid brain region, generated without a) and with b) local field variations due to susceptibility differences. T_2^* map of the latter case shows a reduction in T_2^* around the substantia nigra. c) The difference image of b) subtracted from a). 89

Chapter 1: Introduction

Magnetic Resonance Imaging (MRI) is a widely used, non-invasive imaging technique that provides a means to reveal structural and functional information of different body tissues in detail. A gradient-echo acquisition is used in order to create magnitude and phase images [1]. Magnitude information has been primarily used in MRI for clinical diagnosis due to the soft tissue contrast provided by the images. Depending on the application, a variety of contrasts can be generated between different tissues of interest in the magnitude images by altering the imaging parameters [1]. For example, different contrasts are created by spin density, T_1 and T_2 weighted sequences.

Apart from a few applications such as flow quantification, phase sensitive inversion recovery or MRI thermometry, the phase signal has been ignored in obtaining structural information from different tissues [2-4]. Susceptibility Weighted Imaging (SWI), a relatively new technique in MRI, utilizes the phase information to create filtered phase images that are used to enhance contrast in the magnitude images by using phase information [1-2]. As the phase is dependent on the magnetic susceptibility distribution of a given tissue sample, the phase images offer a unique contrast between tissues. The applications of the phase images include studying the progress of neurodegenerative diseases like multiple sclerosis by detection of iron deposition in the brain, and the

presence of calcium deposition in breast tissue and quantifying oxygen saturation in large blood vessels sometimes using ‘susceptibility maps’ [2, 5, 6].

The phase is a very sensitive tool that provides relevant information about the tissue of interest but due to phase wrapping or phase aliasing along with other local and global field inhomogeneities, there is a need to process the original raw phase images to remove or reduce these effects [1, 7]. Therefore, a clear understanding of the phase behavior is essential to identify normal from abnormal information.

The phase behavior is dependent on the geometry of a given object along with its magnetic susceptibility [2, 6]. Analytical solution for behavior of the phase signal around a cylindrical or a spherical object has been defined in the literature and is often utilized to generate simulated images [1]. The analytical simulation of a cylinder can be used to understand the phase behavior around the blood vessels which are cylindrical in shape, by using the known susceptibility inside the vessels. By altering the main field direction and the radius in the analytical solutions, we can get results which are comparable with the real data [8]. On the other hand, for non-uniform geometries there is no expression that defines the phase outside and inside the object directly even with information about the shape of the object. This makes it difficult to analyze the different structures of the brain which are associated with the diseases studied using phase images.

A three dimensional (3D) brain model is created by extracting various brain structures. By giving susceptibility properties to these structures, the brain model is used to generate simulated susceptibility maps. The susceptibility properties are translated into phase

information using the forward field calculation. This forward method utilizes the Green's function which approximated the dipole function in k-space or Fourier transform of a given object [9-11]. This provides the information about the non-uniform geometries in the brain and helps us to predict the phase around these structures.

The main purpose of this model is to have knowledge about the general phase behavior around the brain structures, such as the basal ganglia that are often associated with analyzing iron deposition and other abnormalities to study the progress of a neurodegenerative disease. As mentioned earlier, removing background field effects in the phase images is the first step to tackle before using them for analysis or any susceptibility mapping procedure. Homodyne high-pass-filtering (HP filtering) of the original raw phase is one of the frequently used methods for this purpose [7]. However, using HP filter can affect the original phase behavior and, therefore, can create false susceptibility distribution when the filtered phase information is used to reconstruct susceptibility maps. The brain model proposed herein will be used to examine the change in phase information caused by the homodyne high pass filter as compared with the unfiltered simulated phase.

Susceptibility mapping utilizes the phase information around an object to reconstruct the susceptibility maps [6]. As in any inversion process, we expect there to be some systematic error as well as changes in SNR. These errors can be predicted by applying the same processing techniques to the simulated phase data generated by using the same imaging parameters as the real data.

By simulating the real life signal imperfections, such as the thermal noise introduced by the MRI scanning apparatus and partial volume effects for small objects due to discretization of the signal when the MR data are sampled through receiver coils, we can simulate realistic phase images [12].

An RF spoiled, short TR, Gradient-Echo (GRE) pulse sequence is generally used for SWI data acquisition [2]. The gradient echo magnitude image is dependent on the tissue T_1 relaxation, T_2^* relaxation and spin density values [1-2]. Therefore, similar to phase simulations, the brain model can be used to produce simulated magnitude images. By varying the echo time, T_2^* maps can be calculated from the simulated magnitude images [13].

Reference:

- [1] Thompson M, Haacke EM, Brown R, Venkatesan R, “*Magnetic Resonance Imaging: Physical Principles and Sequence Design*, Wiley-Liss, 1999.
- [2] Haacke EM, Mittal S, Wue Z, Neelavalli J, Cheng YCN, “Susceptibility-Weighted Imaging: Technical Aspects and Clinical Applications, Part 1,” *American Journal of Neuroradiology*, vol. 30, 2009, pg.19-30.
- [3] De Poorter J, “Noninvasive MRI thermometry with the proton resonance frequency method: study of susceptibility effects,” *Magnetic Resonance in Medicine*, vol. 34(3), 1995, pg.359-367.
- [4] Hou P, Hasan KM, Sitton CW, Wolinsky JS, Narayana PA, “Phase-Sensitive T1 Inversion Recovery Imaging: A Time-Efficient Interleaved Technique for Improved Tissue Contrast in Neuroimaging,” *American Journal of Neuroradiology*, vol. 26(6), 2005, pg.1432-14388.
- [5] Fatemi-Ardekani A, Boylan C, Noseworthy MD, “Identification of breast calcification using magnetic resonance imaging,” *Medical Physics*, vol 36(12), 2009, pg. 5429-5436.
- [6] Haacke EM, Tang J, Neelavalli J, Cheng YC, “Susceptibility Mapping as a Means to Visualize Veins and Quantify Oxygen Saturation,” *Journal of Magnetic Resonance Imaging*, 2010, vol. 32(3), pg.663-676.
- [7] Haacke EM, Xu Y, Change YN, Reichenbach J, “Susceptibility Weighted Imaging (SWI),” *Magnetic Resonance Imaging*, vol. 52, 2004, pg.612-618.

- [8] Shmueli K, de Zwart JA, van Gelderen P, Li TQ, Dodd SJ, Duyn JH, “Magnetic Susceptibility Mapping of Brain Tissue In Vivo Using MRI Phase Data,” *Magnetic Resonance in Medicine*, vol. 62(6), 2009, pg.1510-1522.
- [9] Marques JP, Bowtell R. “Application of a Fourier-based method for rapid calculation of field inhomogeneity due to spatial variation of magnetic susceptibility,” *Concepts in Magnetic Resonance Part B: Magnetic Resonance Engineering*, vol. 25B, 2005, pg.65-78.
- [10] Salomir R, De Senneville BD, Moonen CTW, “A fast calculation method for magnetic field inhomogeneity due to an arbitrary distribution of bulk susceptibility,” *Concepts in Magnetic Resonance Part B: Magnetic Resonance Engineering*, vol. 19B, 2003, pg. 26-34
- [11] Hoffman RE, “Measurement of magnetic susceptibility and calculation of shape factor of NMR samples,” *Journal of Magnetic Resonance*, vol.178, 2006, pg.237-247.
- [12] Cheng YCN, Neelavalli J, Haacke EM, “Limitations of calculating field distributions and magnetic susceptibilities in MRI using a Fourier based method,” *Physics in Medicine and Biology*, vol. 54, 2009, pg.1169–1189.
- [13] Hernando D, Vigen K, Shimakawa A, Reeder S, “ R_2^* Mapping in the Presence of Macroscopic B_0 Field Variations,” *Magnetic Resonance in Medicine*, Accepted 3 November, 2011.

Chapter 2: Basics of MRI Phase signal

The phase, rather than the standard magnitude component, of the Magnetic Resonance Imaging (MRI) signal has been increasingly employed to improve image contrast, and depict normal or abnormal tissues and substructure. This chapter briefly covers the basic concepts related to the phase component of an MRI signal.

2.1 MRI Signal

MRI is a technique based on the interaction of the external main magnetic field with the nuclear spin. One component of this interaction is the precession of the spins about the magnetic field [1]. Nuclear spin is a quantum mechanical intrinsic property of a particle which represents the intrinsic angular momentum of that particle [1].

The frequency of the spin precession around the external magnetic field for a right handed system is given by:

$$\omega_0 = \gamma \cdot B_0 \quad (2.1)$$

where, ω_0 is the frequency of spin precession or the Larmor frequency, γ is the constant known as the gyromagnetic ratio (for a hydrogen proton $\gamma = 2.68 \times 10^8$ rad/s/Tesla) and B_0

Most of the contents of this chapter have been adapted from: Haacke et al, “*Magnetic Resonance Imaging: Physical Principles and Sequence Design*,” 1st Ed., Wiley-Liss;1999.

is the external field strength. In the presence of an external magnetic field, the net magnetization of the spins in a tissue is in the direction of the main field. After a time much larger than the T_1 relaxation time, this magnetization is known as the equilibrium magnetization (M_0) [1]. Even though, the external magnetic field tends to align the protons along the direction of the main field, only a fraction of the total number of spins orient themselves in the direction parallel to the main field.

The three major components of an MRI machine include the ‘main magnet’ that generates a static external magnetic field, the ‘Radio Frequency (RF) coils’ that excite a tissue sample using an RF pulse and receive MRI signal and the ‘gradient coils’ that help in spatial selection of the region of interest [2]. Application of a Radio-Frequency (RF) pulse enables the spin of hydrogen protons to orient away from the main field direction. Due to short temporary presence of this RF pulse, the spin will then collectively precess towards the main field direction [2]. The process of redirecting themselves parallel to the external field is shown in *Figure 2.1*. The decay of the transverse magnetization (magnetization in x-y plane) is called the Free Induction Decay. This helps in regaining the equilibrium state of the magnetization in the presence of the external field, B_0 .

Time-varying magnetic field derived from the sum of all precessing protons spin fields would induce an emf (electro-motive force) which is detected through the corresponding flux changes by a receiver coil, as seen in the *Figure 2.1* [1].

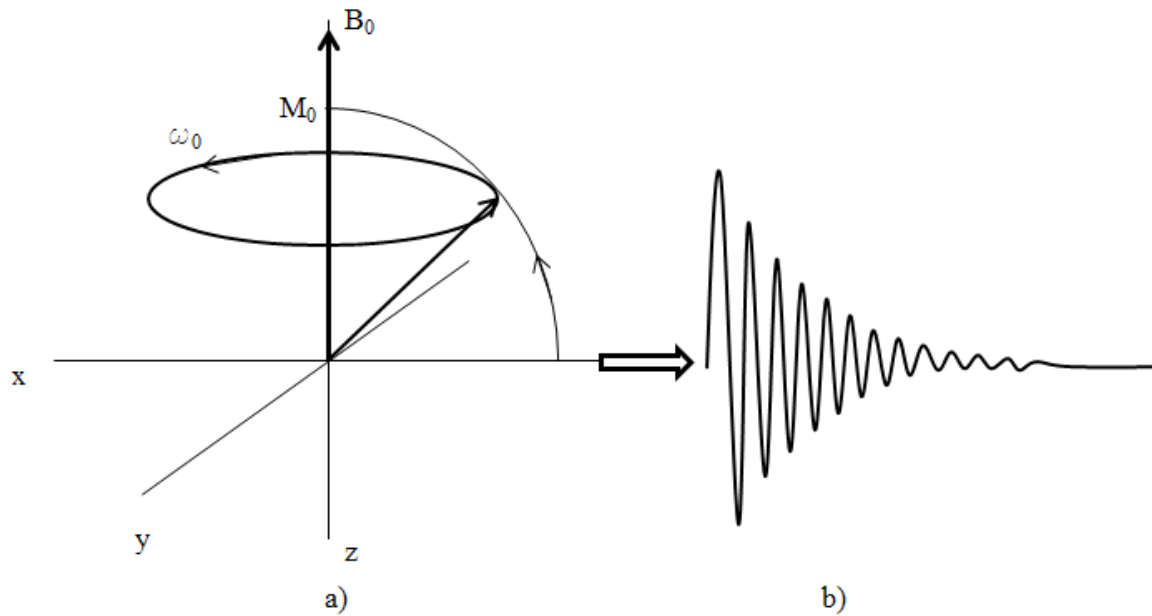


Figure 2.1: *The precession of a spin after the application of an RF pulse, a), which generates an observable NMR signal called free induction decay (FID) signal in the absence of any magnetic gradients, b).*

2.2 Magnetic Susceptibility

Several sources of magnetic field variation can be found in the body which can cause signal distortion, loss of signal, image artifacts and T_2^* losses. Extracorporeal objects include surgically implanted objects, iron-based tattoos, and certain cosmetic products like eye shadows; and also the internal magnetic susceptibility differences found between the tissues in the body [1]. While the extracorporeal objects create distortion artifacts, the internal susceptibility differences can be used to provide a unique contrast in the phase images [3]. This attribute may provide special information about tissues, such as distinguishing lesions from normal tissue [3].

Magnetic susceptibility can be defined as the property of a substance, when placed within an external uniform magnetic field, which measures its tendency to get magnetized and alter the magnetic field around it [1].

The physical magnetic field (measured in Tesla) is given by:

$$\vec{B} = \mu \vec{H} \quad (2.2)$$

where, μ is the permeability constant of the substance and \vec{H} is measured in Ampere/meter (A/m) which is approximately the same as \vec{B} field when there is no substance present [1]. A relative permeability of a substance can be defined as $\mu_r = \mu / \mu_0$, where for free space $\mu = \mu_0 = 4\pi \times 10^{-7} \text{Tm/A}$, a universal constant. The induced magnetic field \vec{B} inside a substance is given by

$$\vec{B} = \mu_0 (\vec{H} + \vec{M}) \quad (2.3)$$

where \vec{M} is induced magnetization serving as a macroscopic source of internal field contribution of the electron spin inside the substance [1].

For a linear material, magnetic susceptibility is viewed as the proportionality constant (χ) for the relation between the induced magnetization in a temporarily magnetized substance and an external magnetic field; and the value of this dimensionless constant describes the magnetic property of the substance [3].

$$\vec{M} = \chi \cdot \vec{H} \quad (2.4)$$

This provides the expression for an induced magnetic field in presence of the external magnetic field and the induced magnetization for a given object with susceptibility χ [1].

Equation 2.2 can be written as:

$$\vec{B} = \mu_0 (1 + \chi)\vec{H}$$

$$\text{and, } \vec{B} = \mu_0 \left(\frac{1+\chi}{\chi} \right) \vec{M}$$

$$\text{Hence, } \vec{M} = \left[\frac{\chi \cdot \vec{B}}{\mu_0(1+\chi)} \right] \approx (\chi \cdot \vec{B})/\mu_0 \quad (\text{when } \chi \ll 1) \quad (2.5)$$

Types of Magnetic Susceptibility:

Substances can be classified into diamagnetic, paramagnetic and ferromagnetic materials based on their macroscopic influence over the external magnetic field [1]. The magnetization depends on the magnetic susceptibility of the object. For empty space, the value of χ is zero, whereas a negative value of χ represents a diamagnetic material, if the value of χ is positive the material is paramagnetic [1]. The terms ‘paramagnetic’ and ‘diamagnetic’ are used relative to the susceptibility of the water rather than vacuum, in MRI field. For ferromagnetic materials, the value of χ is much larger than 1 [1]. The *Equation 2.3* is more suitable equation for the ferromagnetic materials, and, generally, the relevant information for human tissue imaging comes from susceptibility values which are relatively very small [1, 3, 4].

Diamagnetic substances:

Human tissues contain a significant amount of water, making most of the soft tissues diamagnetic in nature. Inert gases, crystal salts, such as NaCl, most organic molecules, and water are some examples of diamagnetic substances. Bone is slightly more diamagnetic than most of the soft tissues in the body [1].

Paramagnetic substances:

Iron is strongly paramagnetic so that even small amounts can be detected [1]. Gadolinium is another good example of a paramagnetic substance and it is combined with a chelating agent to reduce its toxicity, so it can be used in MRI as a contrast agent to depict the vascular network in different regions. Copper, manganese, cobalt, chromium, and dysprosium, are some other examples of paramagnetic ions. Molecular oxygen is also slightly paramagnetic in nature [4].

Ferromagnetic substances:

Ferromagnetic materials, like a horseshoe magnet, can achieve constant magnetization even at a room temperature [4]. Ferromagnetism arises from the individual atomic magnetic moments but results in much stronger induced magnetization, than paramagnetic materials, because of their special structural arrangement. The spins are arranged parallel to each other preferentially, making it a lower energy state. The presence of ferromagnetic materials in human tissues is rare compared to diamagnetic or

paramagnetic substances. Most of the ferromagnetic signals in MRI originate from an external source rather than a biological tissue [4].

2.3 Gradient Echo Imaging

Although, MRI signal is acquired using the receiver coils, the signal is generated using a special set of steps that modify and direct the orientations of spin precession. The free induction decay generates an emf signal [1].

A series of RF pulses are applied to the region of interest which tip the equilibrium magnetization (M_0) away from the external magnetic field and generate a signal, other than the free induction decay, in form of an echo which can be easily acquired by the receiver coils [1]. A pulse sequence is the pattern of applying these RF pulses to generate the desired echo signal, and this pattern varies with the particular type of image to be produced. In MRI, additional external gradient coils are applied to the tissue sample in order to produce spatially dependent signal from a given tissue sample [2].

Gradient coils are used to induce linear variations in the main magnetic field (B_0) (*Figure 2.2a*). There are usually three sets of gradient coils, one for each direction. The variation in the magnetic field permits localization of image slices as well as phase encoding and frequency encoding [2].

Gradient echo (GRE) imaging is one of the most important sequence types used in MRI today. GRE sequence has been used to rapidly acquire MRI data with high spatial resolution and low RF power deposition [5, 6].

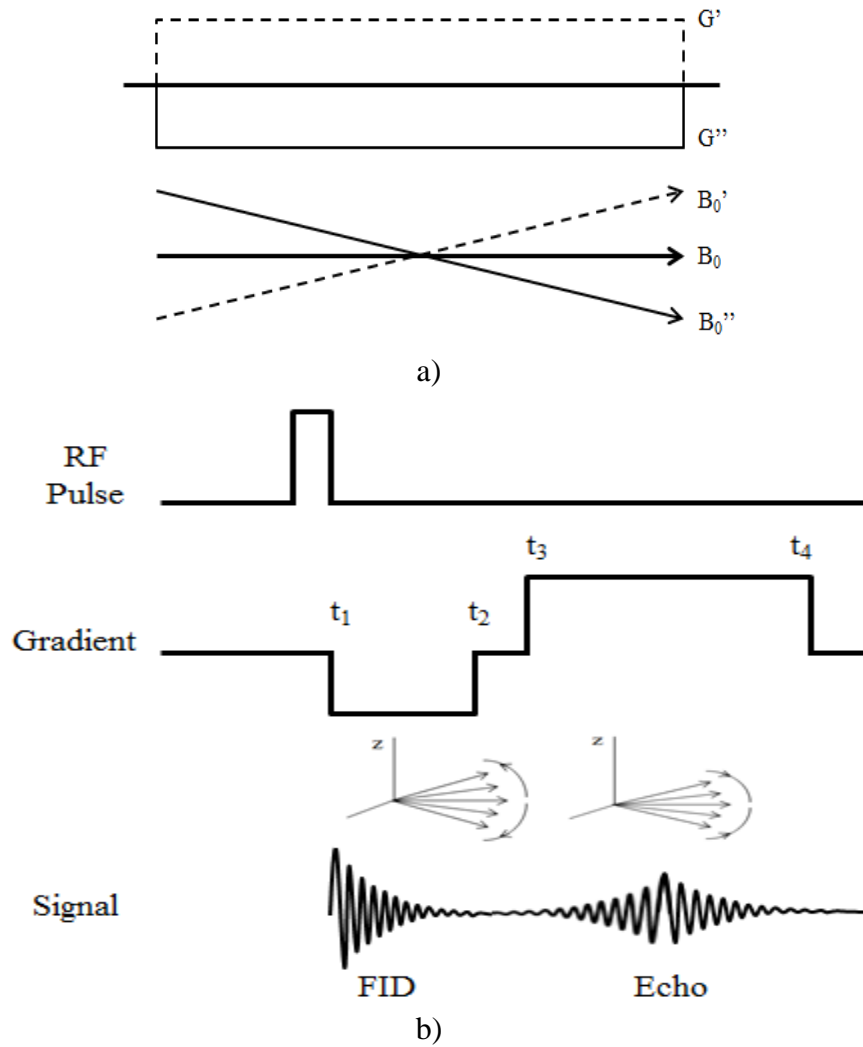


Figure 2.2: Basics of a Gradient echo sequence. a) The effects of applying a positive or negative gradient field in presence of the main external magnetic field (B_0), b) A simple representation of a Gradient Echo pulse sequence.

A simple gradient echo sequence diagram can be seen in *Figure 2.2b*). The RF excitation pulse is followed by a negative gradient signal applied from time t_1 to t_2 along the direction of the main magnetic field (B_0). The net magnetization vector that is tipped onto the transverse plane shows a linear change in precession frequencies (Larmor frequencies) at different z -locations [1]. This can be understood by referring to *Equation*

2.1 that shows the relationship between the precession frequency and the main magnetic field acting on the spin. The presence of a gradient field causes a linear change in the magnetic field with respect to the position in z-direction [2]. The transverse components of spins at different z-locations are shown projected onto the x-y plane below the negative gradient in *Figure 2.2b*) illustrating the dephasing of the signal [2].

Another gradient with reverse polarity is applied to the imaging sample from time t_3 to t_4 . The gradient being opposite in polarity induces rephasing of the signal causing an echo as shown below the positive gradient in *Figure 2.2b*). The time between the RF pulse excitation and maximum gradient echo signal is called the Echo time (TE). This way the gradient echo permits the recovery of the signal using the gradients.

2.4 SWI Pulse Sequence

Gradient echo-based MRI is considered a conventional technique and is routinely used for nearly every medical application in both 2D and 3D data acquisition modes [4]. For Susceptibility Weighted Imaging (SWI) data acquisition, a 3D, RF spoiled, velocity compensated, gradient echo sequence is used (Please refer to *Figure 2.3*) [4]. The signal of this gradient echo sequence also depends on tissue properties like T_1 , T_2^* relaxation times, and the spin density [3]. These properties will be explained briefly in *Chapter 4*. *Gradient moment nulling* (GMN) is a method used to modify a gradient waveform in order to suppress the motion sensitivity of a pulse sequence [2]. Gradient moments are values calculated from the integral of a given gradient waveform with time [2]:

$$m_n = \int [t^n \cdot G(t)] dt \quad (2.6)$$

where, m_n is the n th gradient moment of the gradient waveform $G(t)$. Gradient moments of a gradient waveform can be nulled, depending on the application, to various degrees and orders. Signal variations that lead to artifacts in the image are caused by the rapid and pulsatile flow of blood and cerebrospinal fluid. These artifacts include signal loss due to flow-induced dephasing, misregistration artifacts and the velocity induced phase [1, 2, 4]. The phase for a spin moving with a constant velocity (v) for a bipolar pulse G_x of duration 2τ is given by:

$$\varphi = \gamma \cdot G_x \cdot v \cdot \tau^2 \quad (2.7)$$

Motion or flow with constant velocity is compensated with first order GMN, by nulling the first moment of a gradient waveform, and is also called velocity compensation or flow compensation [2]. For a velocity compensated pulse sequence, the velocity induced phase (given by *Equation 2.7*) disappears, which leaves the desired susceptibility induced phase information [4].

Figure 2.3 represents the original pulse sequence used for SWI data acquisition. A volume with several centimeters of slab thickness is excited using an RF pulse of low flip angle, which is then spatially resolved in 3D space by applying the frequency encoding, phase encoding and partition encoding gradients. Velocity compensation is applied in all three spatial directions- slice-select (G_s), phase-encoding (G_p) and readout (G_r) directions to eliminate oblique flow artifacts [1]. The partition gradients in slice-select and phase encoding directions are rewound after sampling the echo signal, whereas the readout gradient remains to dephase the spins [1].

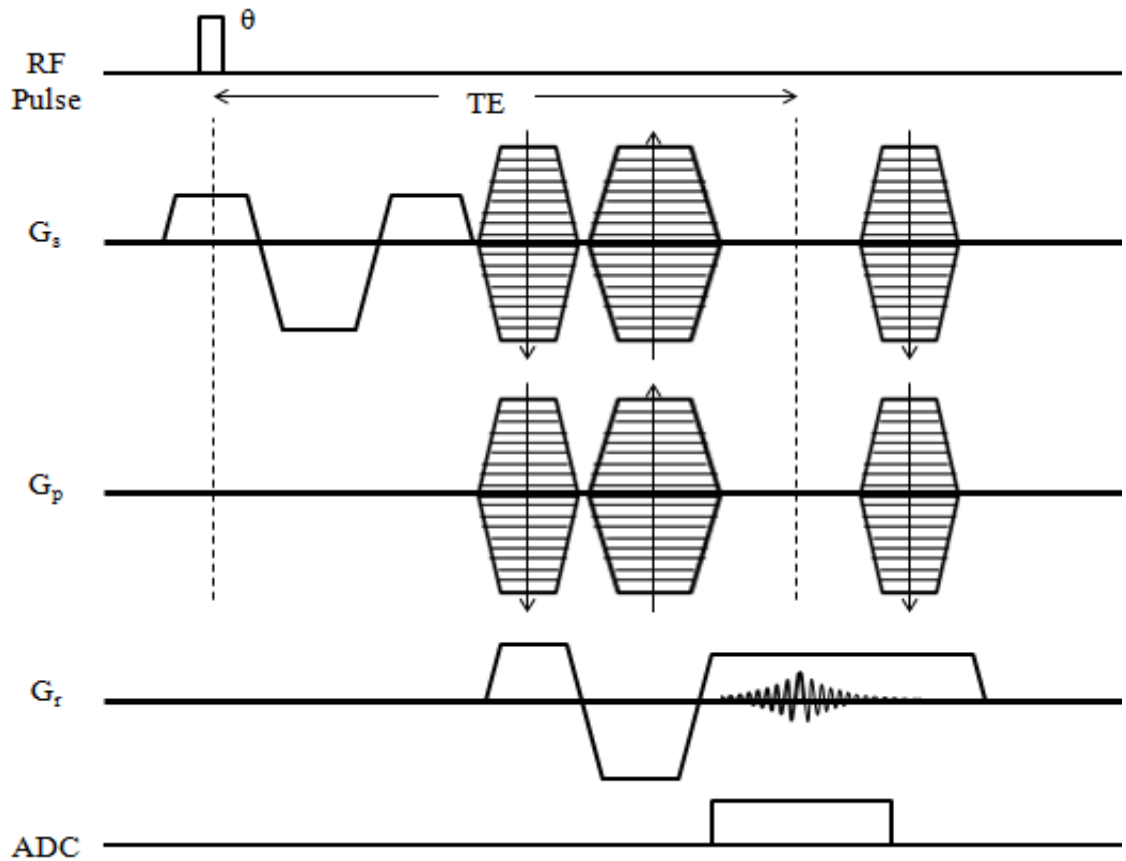


Figure 2.3: *Pulse sequence diagram for a 3D gradient echo MR acquisition with flow compensation in all three directions to reduce the effects of pulsatility effects of the blood or cerebrospinal fluid flow. The pulse sequence includes first order gradient moment nulling in readout (G_r) and slice-select (G_s) directions. The partition encoding and phase encoding (G_p) gradients are velocity compensated with respect to the echo.*

2.5 Complex MR Signal

The two-dimensional precession of the spin in the transverse plane is represented by complex notation [1]. Generally, the signal produced by the rotational motion of the spin precession in presence of a constant magnetic field is acquired by two channels representing real and imaginary parts of a complex signal:

$$S_{xy}(t) = S_x(t) + i S_y(t) \quad (2.8)$$

where, S_x and S_y represent the real and imaginary channels of the signal (Please refer to *Figure 2.4*). This equation can be rewritten as:

$$S_{xy}(t) = |S_{xy}(0)| \cdot e^{i\varphi(\vec{r},t)} \quad (2.9)$$

where, $|S_{xy}| = \sqrt{S_x^2 + S_y^2}$ is the magnitude and $\varphi = \tan^{-1}\left(\frac{S_x}{S_y}\right)$ is the phase component of an MR signal. The phase component of the MR signal is dependent on the position of the spin and the phase accumulation with time [1]. For a right handed system:

$$\varphi(\vec{r}, t) = -\omega_o \cdot t + \gamma(B(\vec{r}))t$$

$$\text{or, } \varphi(\vec{r}, t) = -\gamma(B_o - B(\vec{r}))t \quad (2.10)$$

As seen in the *Equation 2.1*, the phase accumulated at time (t) depends on the larmor frequency (ω_o) and the variations in the main magnetic field due to local variation ($B(\vec{r})$) [4]. The variations in the main magnetic field are introduced by the external linear fields or structural susceptibility effects which are explained later.

2.6 Phase Aliasing

In MR imaging, phase is used to encode spatial information at a position (\vec{r}). However, in addition to the position-dependent phase created by the spatial encoding gradients, there are unavoidably other forms of remnant or background phase present [1, 2]. These

unwanted spurious phase effects also need to be understood and dealt with before useful information from MR phase images can be extracted. A general change of phase over time is studied by simplifying the *Equation 2.10*:

$$\varphi(t) = \Delta\omega \cdot t$$

where, $\Delta\omega$ represents the effective frequency that includes the original larmor frequency and magnetic field variation components.

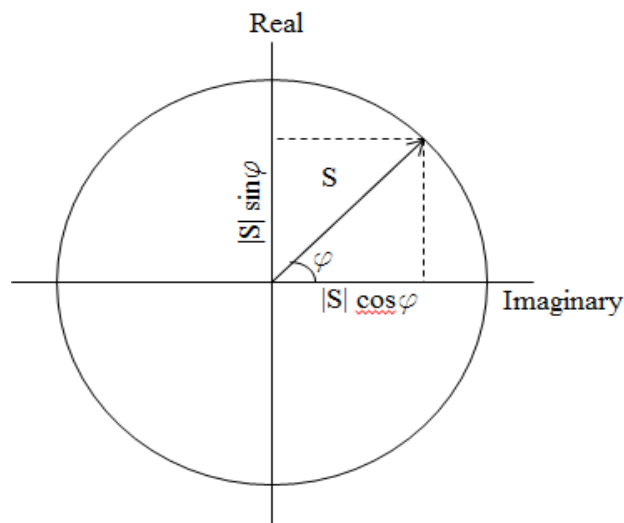


Figure 2.4: *Complex representation of an MR signal acquired through ‘Real’ and ‘Imaginary’ channels. $|S|$ represents the magnitude and φ is the phase component of an MR signal.*

Figure 2.4 shows the phase evolution over time. It is evident that the phase values lie within the range of $-\pi$ to $+\pi$. Therefore, any phase values outside this interval are wrapped back within the interval of $[-\pi, +\pi]$. This phase wrapping is also called phase

aliasing and the aliasing of phase continues as ‘t’ increases (Please refer to *Figure 2.6a*) [1].

2.7 Magnetic Field Perturbations ($\Delta B(\vec{r})$)

The main magnetic field (B_0) should ideally be homogeneous at all the parts of the sample. But, practically, there are local magnetic field variations found in the sample, which can be caused by the imperfect gradient functioning, eddy currents, motion or susceptibility changes between the tissues [1, 3, 4].

As mentioned before, the phase information can be written as a function of the difference between the uniform field B_0 and the local field $B(\vec{r})$ variation at position r and time t .

We can rewrite *Equation 2.10* as:

$$\varphi(\vec{r}, t) = -\gamma(\Delta B(\vec{r})) \cdot t \quad (2.11)$$

where, $\Delta B(\vec{r})$ represents the variation in the main magnetic field due to the presence of local magnetic field. The MR signal is acquired in form of an echo signal, and as mentioned before the time at which the echo is received is represented as TE (Echo time) [1, 2]. Hence, the phase accumulated is given as:

$$\varphi(\vec{r}, t) = -\gamma(\Delta B(\vec{r})) \cdot TE \quad (2.12)$$

The above expression shows the dependence of the accumulated phase signal on the echo time (TE), static main magnetic field (B_0) and the nonhomogeneous, spatially varying, local field distribution ($\Delta B(\vec{r})$).

SWI uses very high spatial resolution and it incorporates the phase into the final image.

The phase difference in the local tissue between the two voxels can be written as:

$$\Delta\varphi = -\gamma \cdot (\Delta B) \cdot TE \quad (2.13)$$

The magnetic susceptibility difference is perhaps the only source at this detail to affect the magnetic field. Due to the high spatial resolution, the background field inside a voxel can be regarded as homogeneous [7]. The magnetic field variations in *Equation 2.13* can be represented as the product of the magnetic susceptibility difference ($\Delta\chi_{diff}$) between the two voxels and the main magnetic field.

$$\Delta\varphi = -\gamma \cdot (\Delta\chi_{diff} B_0) \cdot TE \quad (2.14)$$

The dependence of phase signal on the magnetic susceptibility distribution of a given tissue sample, the phase images offer a unique contrast between the tissue structures such the veins and the surrounding tissue due to the susceptibility difference between the deoxygenated blood in the veins and surrounding tissues is $\Delta\chi \approx 0.45\text{ppm}$ in SI units[3, 4].

Geometric dependence:

The net magnetization in an object within a uniform external magnetic field distorts the uniform field outside the object due to its magnetic susceptibility. The expression of phase difference in *Equation 2.14* shows the phase variation between two voxels due to the susceptibility difference between them, but for a bigger region of interest the field variations can be given as [8]:

$$\Delta B(\vec{r}) = g(\vec{r}) \Delta\chi_{diff} B_0 \quad (2.15)$$

where, g is factor dependent on the geometry of an object. Therefore, the spatial distribution of this deviation in the external applied field is a function of the geometry of the object [8]. The local field deviation inside and around an object is of interest because it gives rise to local phase differences in MR imaging.

$$\text{and, } \Delta\varphi = -\gamma \cdot (g\Delta\chi_{diff} B_0) \cdot TE \quad (2.16)$$

When discussing the effects of geometry on local field variations, we usually neglect the background field and assume that $\chi \ll 1$ [4]. If information of the object shape is analytically known, we can generate the effective phase information inside and outside the object. For example, the effective variations in the magnetic field, calculated using the Lorentz spherical term and Green's function, inside and outside a cylinder that makes an angle θ to the main field are given by [3, 9] (*Figure 2.5*):

$$\Delta B_{in} = \frac{\Delta\chi \cdot B_0(3\cos^2\theta - 1)}{6}$$

$$\Delta B_{out} = \Delta\chi \cdot B_0 \sin^2\theta \cos 2\phi \frac{a^2}{\rho^2} \quad (2.17)$$

where, $\Delta\chi = \chi_i - \chi_e$, χ_i and χ_e are the susceptibilities inside and outside the cylinder, respectively. The derivation of these solutions can be found in literature [1, 9]. The analytical solution for a cylinder can be used to understand the field variations for a blood vessel by using the appropriate susceptibility values.

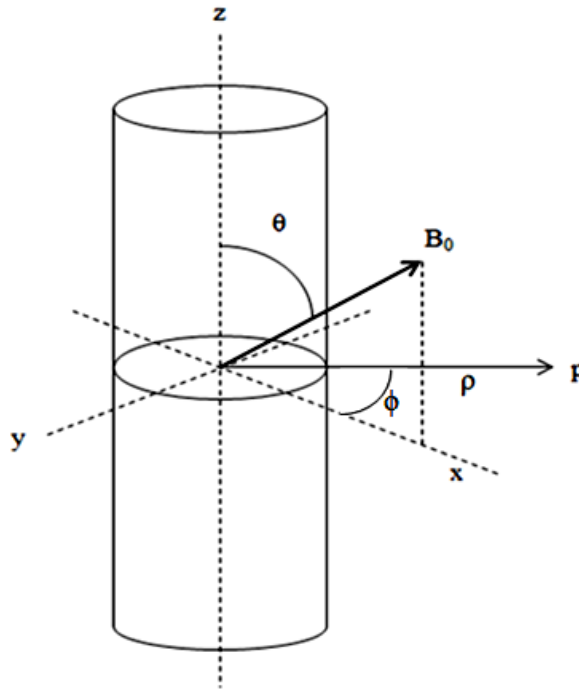


Figure 2.5: A cylinder with a radius ' a ' placed at an angle θ to the external magnetic field B_0 and is the polar angle in the x - y plane of the point ' p ' relative to the external field. The magnetic field variation outside the cylinder at a point ' p ' with a distance ρ can be defined by Equation 2.17.

For more complicated non-uniform structures, the expressions for magnetic field variations around the object are not so straightforward, hence are not available easily [1, 3, 4]. The solution for finding the magnetic field perturbations due to non-uniform geometries will be discussed later in this chapter.

The phase images contain information about all magnetic fields, microscopic and macroscopic. The microscopic field information consists of the local susceptibility distribution and the macroscopic field includes the field changes caused by the geometry of the object, such air-tissue interface around the sinuses in the brain, and by

inhomogeneities in the main magnetic field. The effective phase behavior can be written as the summation of these fields [1, 3, 9]:

$$\varphi = -\gamma(\Delta B_{main\ field} + \Delta B_{CS} + \Delta B_{global\ geometry} + \Delta B_{local\ field}) \quad (2.18)$$

where, ΔB_{CS} represents the field variations due to the chemical shift effects. The field variations due to chemical shift are different from the local field variations due to the susceptibility differences, since the latter depends on the geometry of the object [3].

2.8 Filtered-Phase Images (Homodyne High Pass filter)

In order to remove the field variations due to the inhomogeneities in the main magnetic field and the global geometries such as the sinuses, a Homodyne High pass (HP) filter is applied to the original raw phase images [3, 4, 11].

HP-filtered image, $\rho'(r)$, is obtained by complex dividing the original image $\rho(r)$ by a complex image ($\rho_m(r)$) generated from truncating the central $n \times n$ pixels from the original complex image and zero-filling the elements outside the central $n \times n$ elements to get the same dimensions as the original image.

$$\rho'(r) = \rho(r)/\rho_m(r) \quad (2.19)$$

The central part of k-space, or frequency domain of the complex image, will contain the low frequency spatial changes of the main magnetic field [11]. By generating an image based on the central part of the k-space and complex dividing it from the original

complex data, we should get rid of main field inhomogeneity effects. This would also remove most of the unwanted field variations due to global geometries. *Figure 2.6* shows that most of the low frequency spatially varying fields that obscure the local inter-tissue phase differences of interest are removed after applying the Homodyne high pass filter.

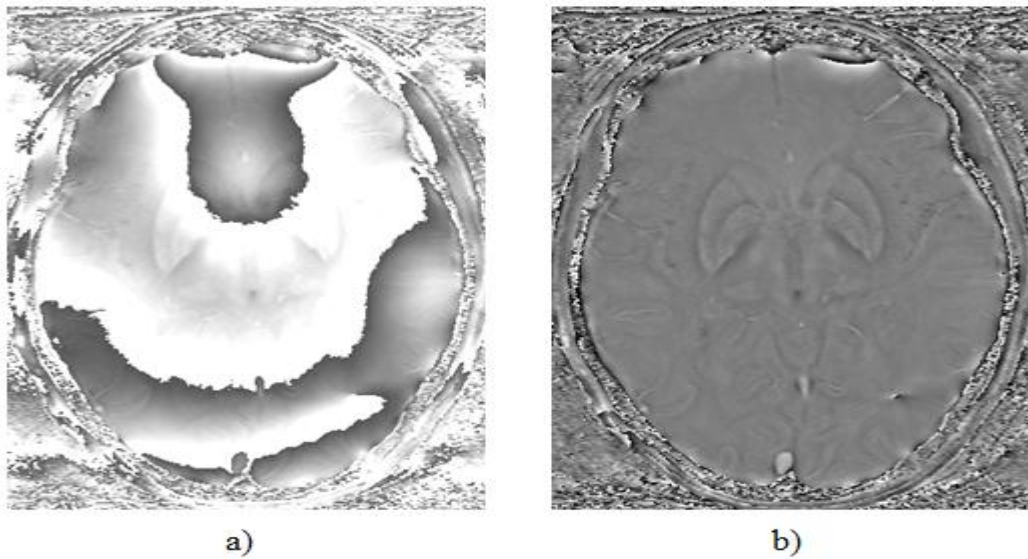


Figure 2.6: *a) Original unfiltered phase image with imaging parameters: $TE=20ms$, $B_0=3Tesla$ with $0.5 \times 0.5 \times 2mm^3$ resolution and b) Homodyne high pass filtered phase image with filter size of 64×64 pixels, which shows the underlying tissue information much clearly by reducing the background field variations.*

The filtered-phase images, with the background field changes almost completely removed in them, have been very helpful in differentiating one tissue from one another, depending on their susceptibilities [4]. However, apart from removing the background field effects, the HP filter also tends to remove some of the physiologically relevant phase information from larger anatomic structures [3, 4]. This limits the use of filter size

larger than 64×64 since it introduces adverse effects on bigger objects with homogeneous distribution of susceptibility values inside them.

2.9 Forward Method for Calculating Field Perturbations

As explained earlier, changes in local magnetic field due to relative differences in biological tissue magnetic susceptibilities can provide a unique tissue contrast. The field variations are dependent on the susceptibility differences and geometry of the object of interest. Hence, methods for estimating this induced static field inhomogeneity due to the presence of an arbitrarily shaped biological tissue in an external homogeneous magnetic field have been of considerable interest right from the early days of MR imaging [12, 13]. Apart from data correction, such methods can also help us better understand the tissue properties observed in MR experiments through better mathematical simulation of the tissue and its properties. Fourier transform-based method used where the induced field perturbation is calculated by convolving the susceptibility distribution with an analytically derived kernel and the method can be rapidly implemented using fast Fourier transform (FFT) algorithms [14, 15].

An object, when placed in an external magnetic field (B_0), develops an induced magnetization, M , owing to its magnetic susceptibility property, χ , as mentioned briefly in the earlier part of this chapter. The z-component of the induced magnetization is in the direction of the main magnetic field therefore it is much larger than x and y components. For linear magnetic materials, the net magnetic field $B_z(\vec{r})$ and induced magnetization $M_z(\vec{r})$ are related by using *Equation 2.5*,

$$M_z(\vec{r}) \approx \frac{\chi(\vec{r})}{\mu_0} B_{0z} \quad (2.20)$$

where, μ_0 is the absolute permittivity of free space. The expression for the resulting net magnetic field distribution at any point ‘r’ due to the presence of induced magnetization $M(\vec{r})$ can be expressed by [4,14,15]:

$$B_z(\vec{r}) = B_0 + \frac{\mu_0}{4\pi} \int_{v'} d^3\vec{r}' \left\{ \frac{3M_z(\vec{r}') \cdot (\vec{z} - \vec{z}')^2}{|\vec{r} - \vec{r}'|^5} - \frac{M_z(\vec{r}')}{|\vec{r} - \vec{r}'|^3} \right\} \quad (2.21)$$

We need to find out the field deviation which can be expressed as $B_{dz}(\vec{r}) = B_z(\vec{r}) - B_0$.

Substituting *Equation 2.20* in the *Equation 2.21* we get,

$$B_{dz}(\vec{r}) = \frac{B_0}{4\pi} \int_{v'} d^3\vec{r}' \left\{ \frac{3\chi(\vec{r}') \cdot (\vec{z} - \vec{z}')^2}{|\vec{r} - \vec{r}'|^5} - \frac{\chi(\vec{r}')}{|\vec{r} - \vec{r}'|^3} \right\} \quad (2.22)$$

The above equation can be expressed as a convolution between the susceptibility distribution and a 3D Green’s function [4]:

$$B_{dz}(\vec{r}) = \frac{B_0}{4\pi} \int_{v'} d^3\vec{r}' [\chi(\vec{r}') \times g(\vec{r} - \vec{r}')] \quad (2.23)$$

$$\text{where, } g(\vec{r}) = \frac{1}{4\pi} \cdot (3\cos^2\theta - r^2) / r^5 \quad (2.24)$$

In the Fourier domain, the Green’s function can be evaluated as [4, 9, 15]:

$$g(k) = \frac{1}{3} - \frac{k_z^2}{k^2} \quad (2.25)$$

where, $k^2 = k_x^2 + k_y^2 + k_z^2$ and k_x , k_y and k_z are the coordinates in k-space. Using the Fourier Transformation (FT) and Inverse Fourier Transform (FT^{-1}), *Equation 2.21* can be rewritten as:

$$\mathbf{B}_{dz}(\vec{r}) = \mathbf{B}_0 \cdot FT^{-1} \left[FT(\chi(\vec{r})) \cdot \left(\frac{1}{3} - \frac{k_z^2}{k_x^2 + k_y^2 + k_z^2} \right) \right] \quad (2.26)$$

The deviations in the magnetic field can now be used to predict the phase behavior using *Equation 2.13*.

$$\phi = -\gamma \mathbf{B}_0 T E \cdot FT^{-1} \left[FT(\chi(\vec{r})) \cdot \left(\frac{1}{3} - \frac{k_z^2}{k_x^2 + k_y^2 + k_z^2} \right) \right] \quad (2.27)$$

The derivation shown above is valid for any arbitrarily shaped, finite, three-dimensional source structure [4, 14]. This expression is utilized on the brain model to simulate the phase images from the susceptibility maps generated for various geometries in the brain.

The continuous Green's function is derived assuming an infinite field of view. However, all the acquired MR data have a finite field of view (FOV) and are discretized. Thus, we always have a discretized object and a finite FOV to begin with while making such field estimation calculations [4]. Hence, to obtain consistent results, a discrete Green's function should be used which is calculated using the finite discrete Fourier transformation of the spatial Green's functions.

The magnetic fields calculated based on a discrete Green's function are aliased (albeit to a lesser degree) in k-space due to finite FOV. The aliasing will increase when the object size increases and becomes comparable to FOV. The problem due to the finite sampling

can be alleviated by increasing the size of the field of view relative to the object size [14, 16]. The forward method can be used accurately even when the object size (i.e., diameter) is as large as 60% of the field of view [4, 9].

2.10 Susceptibility Mapping using Inverse process:

The ability to quantify local magnetic susceptibility makes it possible to measure the amount of calcium or iron in the body whether it is calcium in breast [17] or iron in the form of non-heme iron (such as ferritin or hemosiderin) or heme iron (deoxy-hemoglobin) [3]. Susceptibility maps are produced using the SWI phase data which utilize the information about the phase behavior around the objects to reconstruct the susceptibility distribution in that region [18].

The expression for reconstructing susceptibility distributions can be derived by rearranging the terms in the *Equation 2.27*.

$$\chi(\mathbf{r}) = \frac{FT^{-1}[g^{-1}(\mathbf{k}) \cdot \varphi(\mathbf{k})]}{\gamma \cdot B_0 \cdot TE} \quad (2.28)$$

where $\chi(\mathbf{r})$ is the reconstructed susceptibility map, $\varphi(\mathbf{k})$ is the phase information (filtered or unfiltered), $g^{-1}(\mathbf{k})$ is inverse of the Green's function $g(\mathbf{k})$ given in *Equation 2.25*.

The inverse process, however, produces a region in k-space which consists of unreliable information [18]. This region is defined by the condition when $g(\mathbf{k}) = 0$, i.e. points on or near the conical regions defined by $k_x^2 + k_y^2 - 2k_z^2 = 0$. Thus, the inverse process requires regularization to estimate the susceptibility map. Although constrained regularizations [19, 20, 21, 22] have shown good overall results, they require longer reconstruction times

and assumptions about the contrast around a given object. Threshold-based, single orientation regularization methods (TBSO) [11, 15, 18, 24] provide the least acquisition time and the shortest computational time to calculate SM. However, their calculated susceptibility maps lead to underestimated susceptibility values (χ) and display severe streaking artifacts especially around structures with significant susceptibility differences, such as veins or parts of the basal ganglia like globus pallidus.

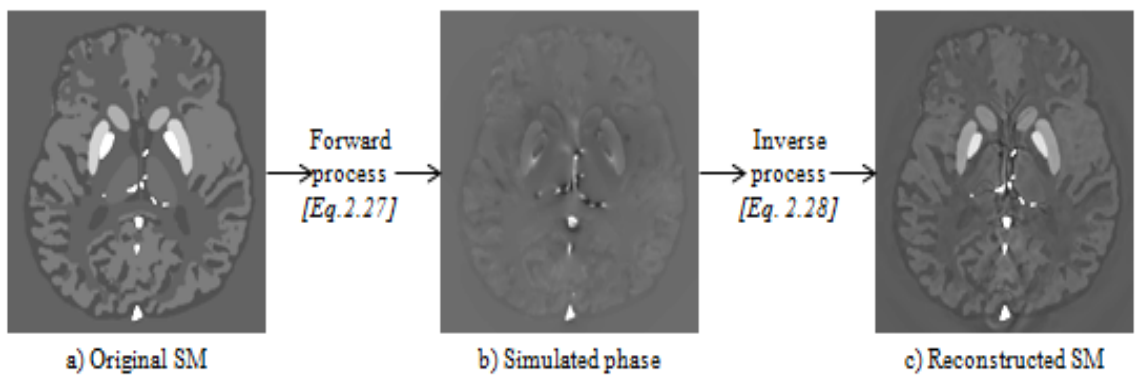


Figure 2.7: *a) Original susceptibility map (SM) of a 3D brain model (Chapter 3), b) Simulated phase generated by using the Forward calculation of the magnetic field perturbations (Please refer to Equation 2.27) at $TE=20ms$ and $B_0=3Tesla$, c) SM reconstructed from phase information in b) using the Inverse process (Please refer to Equation 2.28).*

Figure 2.7 demonstrates a simple example of the Forward and Inverse process to generate simulated phase images and reconstructed susceptibility maps. As we can see, the reconstructed SM is not exactly the same as the original SM (*Figure 2.7a) and 2.7c*). The next chapter introduces a simulated brain model that is used to understand more about the general phase behavior in a human brain and to demonstrate how accurately the transformation of phase to susceptibility takes place.

Reference:

- [1] Haacke EM, Brown R, Thompson M, Venkatesan R, “*Magnetic Resonance Imaging - Physical Principles and Sequence Design,*” *Wiley-Liss*, 1999.
- [2] Bernstein M, King K, Zhou X, “*Handbook of MRI pulse sequences,*” *Elsevier academic press*, 2004.
- [3] Haacke EM, Mittal S, Wue Z, Neelavalli J, Cheng YCN, “Susceptibility-Weighted Imaging: Technical Aspects and Clinical Applications, Part 1,” *American Journal of Neuroradiology*, vol. 30, 2009, pg.19-30.
- [4] Haacke EM, Reichenbach J, “*Susceptibility Weighted Imaging in MRI: Basic Concepts and Clinical Applications,*” *Wiley-Blackwell*, 2011.
- [5] Edelstein WA, Hutchison JM, Johnson G, Redpath T, “Spin warp NMR imaging and applications to human whole-body imaging,” *Physics in Medicine and Biology*, vol. 25, 1980, pg.751–756.
- [6] Haase A, Frahm J, Mathaei D, Haenicke W, Merboldt KD, “FLASH imaging. Rapid imaging using low flip-angle pulses,” *Journal of Magnetic Resonance*, vol. 67, 1986, pg. 258–266.
- [7] Reichenbach J, Venkatesan R, Yablonskiy D, Thompson M, Lai S, Haacke EM, “Theory and application of static field inhomogeneity effects in gradient-echo imaging,” *Journal of Magnetic Resonance Imaging*, vol.7, 1997, pg.266–279.
- [8] Chu SC, Xu Y, Balschi J, Springer CS Jr, “Bulk magnetic susceptibility shifts in NMR studies of compartmentalized samples: use of paramagnetic reagents,” *Magnetic Resonance in Medicine*, vol. 13, 1990, pg. 239-262.

- [9] Cheng YCN, Neelavalli J, Haacke EM, “Limitations of calculating field distributions and magnetic susceptibilities in MRI using a Fourier based method,” *Physics in Medicine and Biology*, vol. 54, 2009, pg.1169–1189.
- [10] Haacke EM, Xu Y, Cheng Y-CN, Reichenbach J, “Susceptibility weighted imaging (SWI),” *Magnetic Resonance in Medicine*, vol. 52, 2004, pg.612–618.
- [11] Wang Y, Yu Y, Li D, Bae KT, Brown JJ, Lin W, Haacke EM, “Artery and Vein Separation Using Susceptibility Dependent Phase in Contrast-Enhanced MRA,” *Journal of Magnetic Resonance Imaging*, vol. 12, 2000, pg.661-670.
- [12] Case TA, Durney CH, Ailion DC, CutilloAG, Morris AH, “A mathematical model of diamagnetic line broadening in lung tissue and similar heterogeneous systems: calculations and measurements,” *Journal of Magnetic Resonance*, vol. 73, 1987, pg.304–314.
- [13] Durney CH, Bertolina J, Ailion DC, Christman R, CutilloAG, Morris AH, Hashemi S, “Calculation and interpretation of inhomogeneous line broadening in models of lungs and other heterogeneous structures,” *Journal of Magnetic Resonance*, vol. 85, 1989, pg.554–570.
- [14] Salomir R, De Senneville BD, Moonen CTW, “A fast calculation method for magnetic field inhomogeneity due to an arbitrary distribution of bulk susceptibility,” *Concepts in Magnetic Resonance Part B: Magnetic Resonance Engineering*, vol. 19B, 2003, pg. 26-34
- [15] Neelavalli J, Cheng YCN, Jiang J, Haacke EM, “Removing Background Phase Variations in Susceptibility-Weighted Imaging Using a Fast, Forward-Field Calculation,” *Journal of Magnetic Resonance Imaging*, vol. 29, 2009, pg. 937–948.

- [16] Marques JP, Bowtell R. “Application of a Fourier-based method for rapid calculation of field inhomogeneity due to spatial variation of magnetic susceptibility,” *Concepts in Magnetic Resonance Part B: Magnetic Resonance Engineering*, vol. 25B, 2005, pg.65-78.
- [17] Fatemi-Ardekani A, Boylan C, Noseworthy MD, “Identification of breast calcification using magnetic resonance imaging,” *Medical Physics*, vol 36(12), 2009, pg. 5429-5436.
- [18] Haacke EM, Tang J, Neelavalli J, Cheng YC, “Susceptibility Mapping as a Means to Visualize Veins and Quantify Oxygen Saturation,” *Journal of Magnetic Resonance Imaging*, 2010, vol. 32(3), pg.663-676.
- [19] Kressler B, de Rochefort L, Liu T, Spincemaille P, Jiang Q, Wang Y, “Nonlinear regularization for per voxel estimation of magnetic susceptibility distributions from MRI field maps,” *IEEE Transactions on Medical Imaging*, vol. 29, 2010, pg.273-281.
- [20] Liu T, Liu J, de Rochefort L, Spincemaille P, Khalidov I, Ledoux JR, Wang Y, “Morphology enabled dipole inversion (MEDI) from a single-angle acquisition: Comparison with COSMOS in human brain imaging,” *Magnetic Resonance in Medicine*, vol. 66, 2011, pg.777-783.
- [21] de Rochefort L, Liu T, Kressler B, Liu J, Spincemaille P, Lebon V, Wu J, Wang Y, “Quantitative susceptibility map reconstruction from MR phase data using Bayesian regularization: validation and application to brain imaging,” *Magnetic Resonance in Medicine*, vol 63, 2010, pg.194-206.
- [22] Li Y, Xu N, Fitzpatrick JM, Morgan VL, Pickens DR, Dawant BM, “Accounting for signal loss due to dephasing in the correction of distortions in gradient-echo

EPI via nonrigid registration,” *IEEE Transactions on Medical Imaging*, vol. 12, 2007, pg.1698-1707.

- [23] Wharton S, Schafer A, Bowtell R, “Susceptibility mapping in the human brain using threshold-based k-space division,” *Magnetic Resonance in Medicine*, vol.63, 2010, pg.1292-1304.
- [24] Shmueli K, de Zwart JA, van Gelderen P, Li TQ, Dodd SJ, Duyn JH, “Magnetic susceptibility mapping of brain tissue in vivo using MRI phase data,” *Magnetic Resonance in Medicine*, vol. 62, 2009, pg.1510-1522.
- [25] Grabner G, Trattnig S, Barth M. Filtered deconvolution of a simulated and an in vivo phase model of the human brain. *Journal of Magnetic Resonance Imaging*, vol. 32, 2010, pg.289-297.

Chapter 3: A Three Dimensional Model of the Brain

A three dimensional (3D) model of the brain is developed to interpret the simulated phase behavior with the real phase images and to evaluate the accuracy of various susceptibility mapping methods. SWI phase images are useful in obtaining edge information for some of the anatomical structures in the brain. These susceptibility changes have been used as a biomarker to study the progress of neurodegenerative diseases, such as multiple sclerosis, where iron deposition correlates with a low signal in the region of interest [1].

A scientific model of a system can be described as a mathematical and/or computational estimate which is used in the construction, experimentation, validation and even modification of the scientific theories based on the integrated previous knowledge related to a given system [2]. The brain model represents the key characteristics of the system, such as the magnetic susceptibility property of the tissues and the geometrical information of the brain structures, by which the phase response is generated. The simulations produced from this brain model represent the outcome of the system, in which the parameters are modified so as to be compared with real life data. These modifications include the time at which the MRI signal is collected, i.e. echo time (TE), and the main magnetic field strength (B_0), both of which are important parameters of phase information (φ):

$$\varphi = -\gamma \cdot \Delta B(\vec{r}) \cdot TE \quad (3.1)$$

where, γ is the gyromagnetic ratio and $\Delta B(\vec{r})$ represents the local magnetic field perturbations. The magnetic field perturbations are calculated, for a given non-uniform geometry, using the Forward method [3- 5]. The key point is that susceptibility differences between two adjacent structures lead to a spatial field deviation within and around them, which is a function of their geometries (as explained in *Chapter 2*). Confounding factors like the thermal noise (Signal-to-noise ratio (SNR) in an image) and partial volume effects (due to the discrete sampling in the MR signal) will also be incorporated in the simulations to study their effects, making the simulations more realistic.

This chapter will discuss the role of this model in analyzing the post-processing techniques used on the real phase images to generate filtered phase images and susceptibility maps.

3.1 Structures of the Brain Model

The model includes the red nucleus, substantia nigra, crus cerebri, thalamus, caudate nucleus, putamen, globus pallidus, vessels, grey matter, white matter in the cerebral cortex and the cerebellum along with cerebrospinal fluid (CSF). In order to model these structures, it is essential to have prior information about them.

3.1.1 Basal ganglia:

The basal ganglia of the human brain mainly consist of the caudate nucleus, putamen and globus pallidus which have neural connections with substantia nigra and red nucleus.

These neural structures are found buried deep inside the cerebral white matter [6]. The structures are primarily involved in coordinated voluntary movement control, response selection and initiation [6, 7].

3.1.1a) Caudate nucleus:

The caudate nucleus is a nucleus located within the basal ganglia located near the center of the brain, sitting astride the third ventricle; situated in both the hemispheres of the brain [7]. The shape of the caudate nucleus includes a wider head region and it narrows down towards its tail. The intermediary region is considered as the body of caudate nucleus.

3.1.1b) Putamen:

On an axial plane, the putamen is the most lateral structure of the basal ganglia, and together with the caudate nucleus it is referred to as the dorsal striatum [7]. Medially it abuts the globus pallidus and laterally it is surrounded by the external capsule. The putamen, together with the globus pallidus, makes up the lenticular nucleus [7].

3.1.1c) Globus pallidus:

The globus pallidus is located medially to the putamen, found in both hemispheres of the brain. The globus pallidus receives input from the putamen and caudate nucleus and outputs the information to the substantia nigra [7].

3.1.1d) Thalamus:

The thalamus is another symmetrical structure which is found next to the midline of the brain made by the narrow third ventricle. Laterally, it is surrounded by the internal capsule, and it is situated between the cerebral cortex and midbrain [8].

3.1.1e) Substantia nigra:

The substantia nigra is located in the upper portion of the midbrain [7]. It is the largest nucleus in the midbrain and is divided into two parts: the pars reticulata (SNr) and pars compacta (SNc), which lies medial to the pars reticulata.

3.1.1f) Red nucleus:

The red nucleus is a structure in the rostral midbrain next to the substantia nigra involved in motor coordination.

3.1.1g) Crus Cerebri:

The crus cerebri is located laterally to the substantia nigra and it generally shows a diamagnetic property.

Iron deposition in the basal ganglia is of interest in studying neurodegenerative diseases such as Multiple Sclerosis [10]. Substantia nigra is one of the primary sources of dopamine synthesis and the increase in iron accumulation, which is involved in the dopaminergic pathways to a great extent, is observed in the pars compacta in Parkinson's disease [11]. The crus cerebri, which is known to be related with coordinating motor control, is studied along with the substantia nigra in Traumatic Brain Injury (TBI) cases. Abnormal iron metabolism in the brain is typified by Hallervorden-Spatz syndrome; large amounts of iron are seen deposited in the globus pallidus and the pars reticulata of the substantia nigra [12].

Extraction of Basal Ganglia:

Fully velocity compensated, RF-spoiled, high resolution, 3D gradient echo SWI-magnitude and phase images, with imaging parameters: TE=18ms, TR=27ms, FA=15°, B0=3T and (0.5mm)³ isotropic resolution, are used to obtain the structures in basal ganglia region. Extraction is done manually by drawing contours of the boundaries identified in real phase images. Susceptibility maps of this real data, generated by using the inverse of the Green's function, were used to distinguish the structures from its dipole effect produced in phase images [13] (Please refer to *Figure 3.1*).

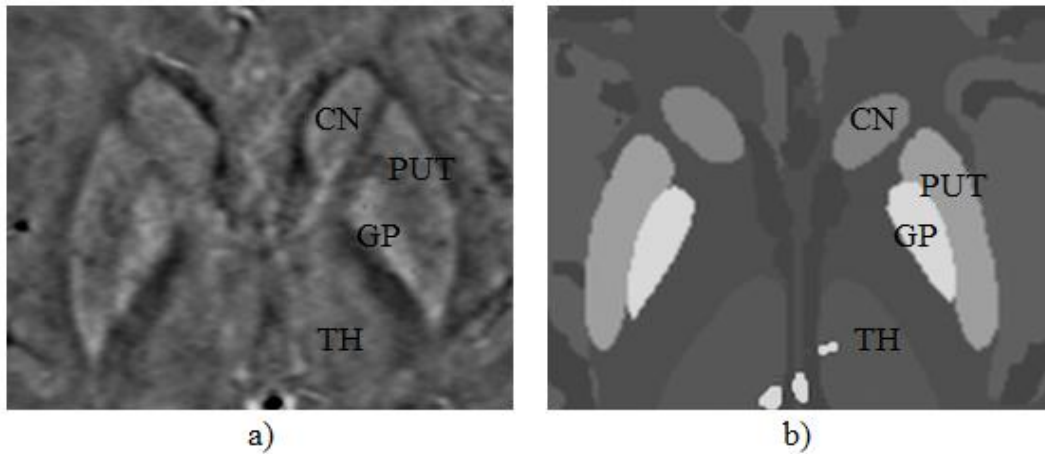


Figure 3.1: a) Susceptibility map of the real data with imaging parameters: $TE=20ms$ and Main field strength=3Tesla, b) Simulated susceptibility map produced by extracting the basal ganglia structures. CN=Caudate Nucleus, PUT=Putamen, GP=Globus Pallidus, TH=Thalamus. Please refer to **Figure 3.11** for the structures in mid-brain.

Care was taken to remove any uneven jagged edges, by making the boundary of the geometries more homogeneous, in axial, coronal and sagittal planes, to avoid creating unwanted dipole effects. These dipole effects can create false contrast in the phase images and can be misunderstood as the presence of paramagnetic substances. If this were misinterpreted as iron deposition by a clinician, it could change the diagnosis and possibly even treatment of the patient in a negative way.

3.1.2 White matter and Grey matter:

In order to make the model more realistic, it is important to add white matter and grey matter. Adding signal from background tissues, like white matter, grey matter and

cerebro-spinal fluid, will help in understanding the phase around the structures of basal ganglia more accurately.

White matter forms the bulk of the deep parts of the brain and the superficial parts of the spinal cord. Cerebral white matter encapsulates the deep grey matter structures like basal ganglia and brain stem nuclei. The cerebellum consists of the superficial layer of the cerebellar cortex which covers the underlying deep cerebellar white matter, also known as the "arbor vitae") [7]. The cerebral ventricles, i.e. lateral ventricles, third ventricle, cerebral aqueduct, fourth ventricle are located deep within the cerebral white matter.

White matter fibers act as a relay between different areas of gray matter within the nervous system. Multiple Sclerosis (MS) is one of the most common diseases which have been correlated with the axonal loss and iron deposition in white matter lesions [14].

In contrast to the white matter, **grey matter** contains neural cell bodies, instead of myelinated axonal fiber tracts [9]. Grey matter is located at the surface of the cerebral hemispheres and of the cerebellum (cortex). Deep grey matter nuclei include the basal ganglia, cerebellar nuclei and brain stem nuclei [7].

Cerebro-spinal fluid (CSF) is found in the ventricles of the brain, sulci of grey matter and the subarachnoid spaces [8]. The main functions of CSF are to protect the cortex of the brain from injuries to the skull and provide immunological protection to the brain. It also increases the intracranial pressure in the brain, leading to a greater brain perfusion and preventing ischemia to brain tissues.

Extraction of white matter, grey matter and cerebrospinal fluid:Double inversion recovery (DIR) sequence:

The DIR sequence is used to nullify signal related to a particular tissue, i.e. white matter or grey matter and CSF. Double Inversion Recovery (DIR) MRI utilizes two radio-frequency inversion pulses in order to nullify signals from the desired tissues, depending on their longitudinal relaxation times [14]. In the brain, DIR makes it possible to selectively image grey matter (GM) by nulling the signal from white matter (WM) and cerebrospinal fluid (CSF) at the time of the excitation pulse [16].

For GM, WM and CSF extraction, two double-inversion recovery (DIR) sequences, one with WM suppression (DIR₁: TE=1.46ms, TR=3100ms, 3T) and another with GM and CSF suppression (DIR₂: TE=1.57ms, TR=2800ms, 3T), are used.

DIR₂ is used to remove WM efficiently in order to isolate GM and CSF. GM and CSF are separated by using a local thresholding method on DIR₁ to isolate GM and CSF with the help of the intensity difference between them [17].

A WM mask is created by subtracting the GM, CSF and basal ganglia structures from the geometry of the whole brain. GM, CSF and WM masks were created with 0.5*0.5*2mm resolution, which is interpolated in k-space by zero padding (in main field direction) to get (0.5)³ mm data (Please refer to *Figure 3.2*).

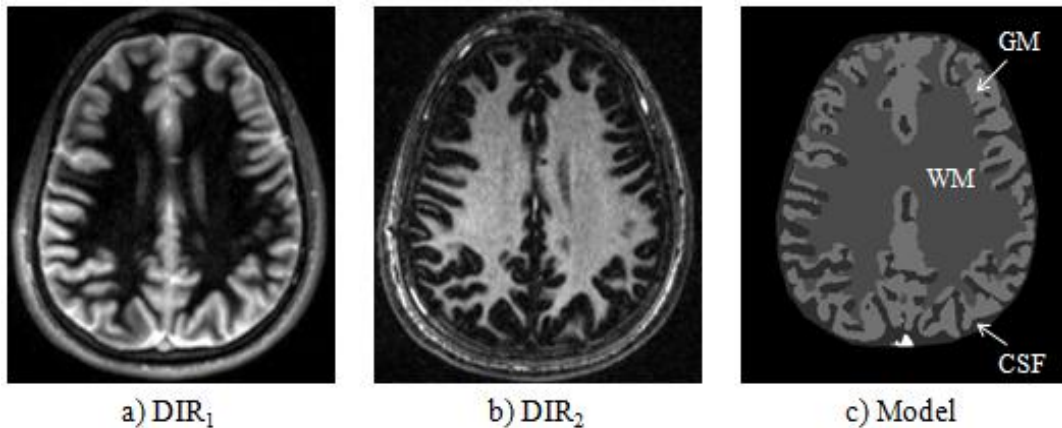


Figure 3.2: Segmentation of grey matter (GM), white matter (WM) and cerebrospinal fluid (CSF) using Double Inversion Recovery (DIR) sequences. DIR_1 ($TE=1.46ms$, $TR=3100ms$, $3T$) suppresses WM signal whereas DIR_2 ($TE=1.57ms$, $TR=2800ms$, $3T$) suppresses signals of GM and CSF. The image c) shows the brain model with the segmented GM, WM and CSF tissues.

3.1.3 Cerebellum:

The cerebellum is involved in the coordination of voluntary motor movement, balance and equilibrium and muscle tone. It is located just above the brain stem and toward the back of the brain. It is relatively well protected from trauma compared to the frontal and temporal lobes and brain stem.

The convoluted surface of the cerebellum consists of a tightly folded layered cerebellar cortex. White matter is found below the cerebellar cortex. Embedded within the white matter are four deep cerebellar nuclei, fastigial, emboliform, globose, and dentate, which are not yet included in the model [18].

Extraction of Cerebellum:**T1-Weighted MPRAGE sequence:**

The MPRAGE (Magnetization Prepared Rapid Gradient Echo) sequence has been used often for its excellent grey/white matter contrast [19]. A preparatory pulse with a flip angle ranging from 0-180° is applied to a desired field of view (FOV) followed by a gradient echo sequence. T₁ contrast is introduced into the longitudinal magnetization after a delay time (TI). The MRI signal is then acquired from this T₁-prepared magnetization [20]. This sequence allows rapid 3D acquisition with dominant T1 weighting.

In order to be able to extract both the cerebellar cortex and white matter, T1 weighted MPRAGE sequence data, with imaging parameters: TE=2.26ms, TR=1950ms, TI=900ms, B₀=3Tesla, Flip-angle=9° with pixel resolution of 0.5×0.5×1mm, was used. The extraction was done using local thresholding for white matter and then for the cerebellar cortex [17]. The segmented cerebellum was transformed from the resolution of 0.5×0.5×1mm³ to 0.5×0.5×0.5mm³ by using k-space interpolation. The values inside the white matter and the cortex were later made constant to provide homogenous susceptibility distribution.

3.1.4 Venous network:

Homodyne high pass filtered phase images have been used to enhance venous signal [13, 21]. Phase images are known to show high contrast for the veins due to the higher

susceptibility difference of the veins with respect to surrounding tissues ($\Delta\chi\approx 0.45\text{ppm}$) [22]. This contrast also depends on the amount of the deoxy-haemoglobin, a paramagnetic substance, carried by the veins. Phase provides a means to calculate the oxygen saturation in the blood vessels from the susceptibility maps [13].

Extraction of veins:

A vessel map is extracted from the susceptibility maps from SWI phase images. The higher susceptibility values of the veins in the susceptibility maps makes it possible to use a simple threshold approach to extract most of the prominent veins in the brain, namely the vein of Galen, internal cerebral veins, thalamo-striate veins, septal veins, medial veins, and superior sagittal sinus along with the straight sinus. The vessel masks for each vein were made continuous and smooth in all three planes to avoid creating false contrast in the phase simulations caused by the unwanted dipole artifacts.

3.2 Validation of the extracted structures

Validation of the shape and positions of the structures are done with the help of literature material on anatomy of the brain structures. A symmetrical model was created with a 3D matrix with resolution of $0.5\times 0.5\times 0.5\text{mm}^3$ [7, 9, 18].

The susceptibility distribution inside the structures is defined by an appropriate value and the edges of the structures are not smoothed or altered; this defines a proper homogeneous susceptibility distribution for the structures. The shapes of the basal

ganglia structures are further validated by comparing them with the Human Subcortical Atlas available on the internet courtesy of Johns Hopkins University (Please refer to *Figure 3.3*). The atlas was created by using data from 41 subjects to segment caudate nucleus, hippocampus, globus pallidus, putamen thalamus and ventricles. A template was generated from 41 subjects for each structure using Large Deformation Diffeomorphic Mapping (LDDMM) technique [23].

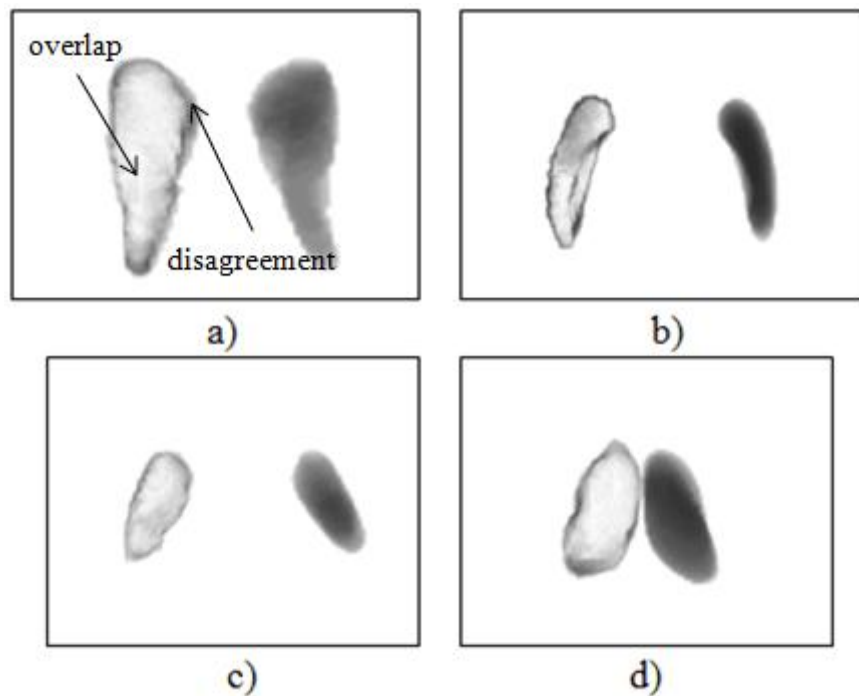


Figure 3.3: Validation of the extracted structures using Human Subcortical Atlas made by Johns Hopkins University (JHU). a) Caudate nucleus, b) Putamen, c) Globus pallidus, d) Thalamus. The white region in the left-half of each structure shows the overlap region between the extracted structure for the brain model and the JHU atlas. The right-half of the figures represents the extraction of the structures for the model and is given for your reference. These images are generated by volume rendering using the Volview3.4 © software, Kitware Inc. Please note that the variations seen at the edges are due to the smoothed profile at the edge of the atlas structures. The model consists of

homogeneous susceptibility distribution inside the structures without any rough boundary that could create false dipole effects.

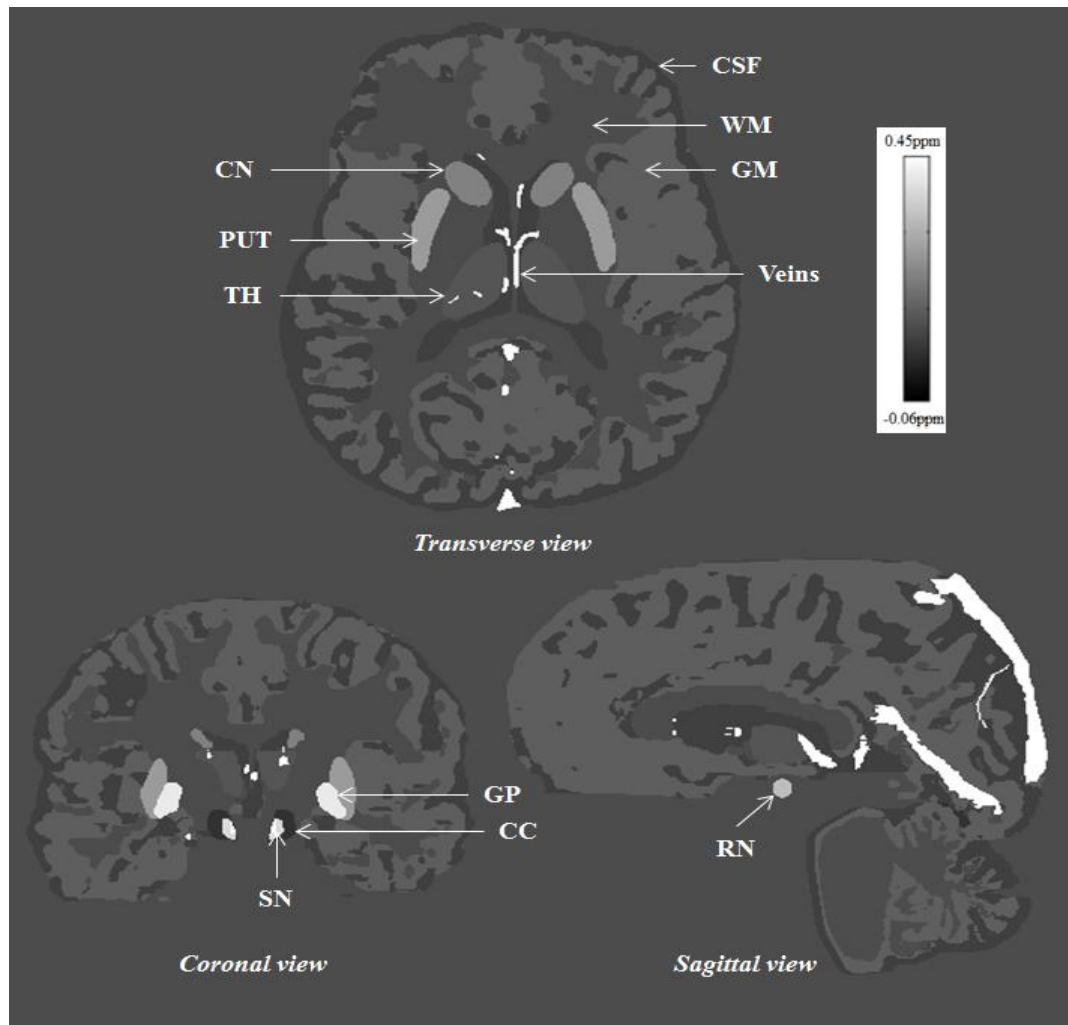
The brain model, thus, produced is to be utilized as a generalized model of the structures. Relative positions of the structures will vary for different individuals, and this inter-individual variability is expected. The knowledge of the general shape and positions of the structures in the brain model helps to study a general phase behavior of the structures relative to each other in the same 3D space.

Subsequently, a graphic-user interface is created using MATLAB2009a© (Mathworks Inc.) to be able to assign desired imaging parameters: echo time, field strength and resolution to the model, with desired susceptibility values to each aforementioned structure. Susceptibility values in parts per million (ppm) for the structures SN, RN, PUT and GP, were taken from ref. [27] and others were from measuring the mean susceptibility value in a particular region from susceptibility maps using ref. [13] from in vivo human data (in ppm): RN = 0.13, SN = 0.16, CC = -0.03, TH = 0.01, CN = 0.06, PUT = 0.09, GP = 0.18, vessels = 0.45, GM = 0.02, CSF = -0.014 and WM=0. Susceptibility changes are reported relative to white matter as the origin (0ppm). A negative susceptibility value indicates that the structure is more diamagnetic with respect to the white matter, such as CSF. From this point onwards, all the simulations will be done using these susceptibility values for the structures.

Human Brain Atlases:

There are other subcortical atlases of the human brain available for MRI data including: the Talairach atlas, the MNI (McConnell Brain Imaging Centre, Montreal Neurological Institute) brain and the Human-subcortical-atlas from John Hopkins University (JHU) [23, 24, 25]. These models contain structures that are defined after they are averaged across a several cases. This provides more accurate shape and positional information about the structures, but the intensity inside them is not homogeneous due to normalization or affine transformations.

Another high resolution (0.5mm isotropic) brain model, Colin27, is made from T1, T2 and PD weighted images formed from the average of 27 scans from the same subject [26]. The ‘Colin27’ model provides the extracted grey matter, white matter and vessels. However, this model does not provide separate subcortical structure models. The edge information is generally well defined in the phase images when the susceptibility difference is significant. This is the main reason of utilizing real phase images to extract the basal ganglia structures. As mentioned before, other MRI image types like magnitude images, 3D MPRAGE T1 weighted images and susceptibility maps were used as a reference to the extractions.



Structure	χ value (in ppm)	Structure	χ value (in ppm)
White matter	0	Veins	0.45
Grey matter	0.02	Red Nucleus	0.13
Globus Pallidus	0.18	Substantia Nigra	0.16
Putamen	0.09	Thalamus	0.01
Caudate Nucleus	0.06	Crus Cerebri	-0.03
Cerebrospinal Fluid	-0.014		

Figure 3.4: Transverse, Coronal and Sagittal views of the three-dimensional brain model. The structures are differentiated by their susceptibility values which are listed in the table below the image. CN=Caudate nucleus, SN=Substantia nigra, RN=Red nucleus,

GP=Globus pallidus, CC=Crus Cerebri, PUT=Putamen, TH=Thalamus, WM=White matter, GM=Grey matter, CSF=Cerebrospinal fluid, and veins.

3.3 Applications of the Brain Model

The model is developed to mimic the phase behavior of various brain structures and analyze the processing techniques used on real phase images to create susceptibility maps. Using the geometry information and susceptibility properties for different structures as the parameters, this model is used to simulate phase images. Phase information around these structures is generated using a Forward method, as explained in *Chapter 2.9*. The forward method calculates magnetic field perturbations from convolution of the simulated susceptibility map and the Green's function $[g(k)]$ representing a dipole kernel.

The expression of simulated phase (φ) is given as:

$$\varphi = -\gamma B_o TE \cdot FT^{-1}\{FT[\chi(r)] \cdot g(k)\} \quad (3.2)$$

where, $\chi(r)$ is the 3D model of the brain with susceptibility properties given to different tissues, $\chi(r)$ and $g(k)$ are both of same dimensions, FT and FT^{-1} represent Fourier Transformation and Inverse Fourier Transformation respectively.

Zero filling:

Although the phase simulation shows the ideal behavior related to the brain structures, the Forward filter works by assuming there is infinite field-of-view (FOV). Hence, there is some remnant phase aliasing back inside the images due to limited FOV. To reduce this effect, zero filling or zero padding is done in all the directions to increase the FOV to $512 \times 512 \times 512$ with the isotropic resolution of $(0.5\text{mm})^3$. Smaller FOV can produce significant aliasing back into the phase image, even inside the brain; causing unavoidable changes in the phase information [28]. This change leads to erroneous results in quantifying the susceptibility value from the reconstructed susceptibility distribution maps [28].

3.3.1 Analysis of Phase Processing Techniques

One of the main applications of this 3D model of the brain is to validate different processing techniques currently used for the real MRI phase images. The expression of simulated phase (φ) is given by Equation 3.2 with TE= 20msec, B0=3T are selected.

3.3.1a) Homodyne High Pass filter:

Removing background field effects and phase wrapping in the phase images is the first step to tackle before using them for analysis and susceptibility mapping. Homodyne high-pass-filtering (HP filtering) of the original raw phase is one of the frequently used

methods for this purpose (See *Chapter 2.8*). Susceptibility maps produced from these filtered phase images are widely used to quantify iron deposits or calcium deposits in a given tissue [13].

However, using Homodyne HP filter can affect the accuracy of determining the region of interest for quantification since it leads to a loss of low frequency phase information. The brain model can be used to evaluate the accuracy of the susceptibility maps after applying the Homodyne HP filter of various sizes.

The results of HP filtering are then compared with results obtained using a different processing technique known as SHARP (Sophisticated Harmonic Artifact Reduction on Phase data). SHARP is another method that is used to remove the background field variations [29]. This method works on the principal that the background field variations can be approximated as a ‘harmonic’ component of the phase data in the region of homogeneous susceptibility. The harmonic component of the data satisfies the Laplace’s equation. The phase data can be differentiated between the heterogeneous susceptibility, where the field is non-harmonic, and homogeneous susceptibility, where the field is harmonic. The harmonic component has a property that it is invariant when convolution is done using a normalized spherical shell. This helps in removing the harmonic component from the phase data [29].

In order to test the effects the filtering techniques, other image distortions like external white Gaussian noise and partial volume effects due discrete sampling of the MR signal

are not introduced. These image imperfections will be covered in the later part of the chapter.

The profile plot seen in the *Figure 3.5-d* explains the change in phase behavior, across the lenticular nucleus, introduced by the Homodyne high pass filter of size 64×64 and SHARP technique (kernel radius=6). As compared to original phase image, Homodyne high pass filter introduces a considerable change in the phase information including a shift in baseline of the phase distribution. On the other hand, SHARP processed phase tends to preserve the phase information better than HP filtered phase images.

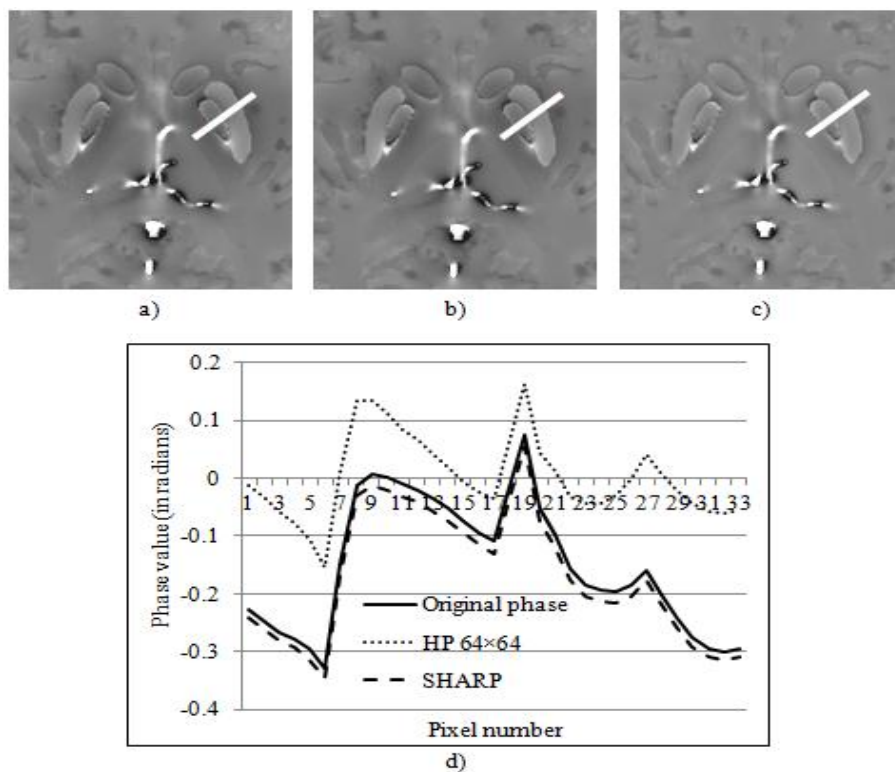


Figure 3.5: Comparison of MRI real phase information processing techniques using a 3D brain model. a) Original phase image (imaging parameters $TE=18ms$ and $B_0=3T$), b) Homodyne High pass filtered phase image (filter size 64×64 pixels), c) SHARP

processed phase image. Graph d) shows the profile plot of the phase distribution across the lenticular nucleus (putamen and globus pallidus) along the white-bar in a), b) and c).

The inverse filter (as explained in Chapter 2.9) is used to generate susceptibility maps from the phase data. The susceptibility values measured from susceptibility maps for the different structures are a function of the HP filter size (8×8, 16×16, 32×32, 64×64, 96×96, 128×128 pixels) and SHARP technique (as seen in the *Figure 3.6*). As compared to the original susceptibility value, the error in the quantified susceptibility value increases as HP filter size increases. The error introduced by SHARP technique is slightly more than a small sized high pass filter (8×8 pixels).

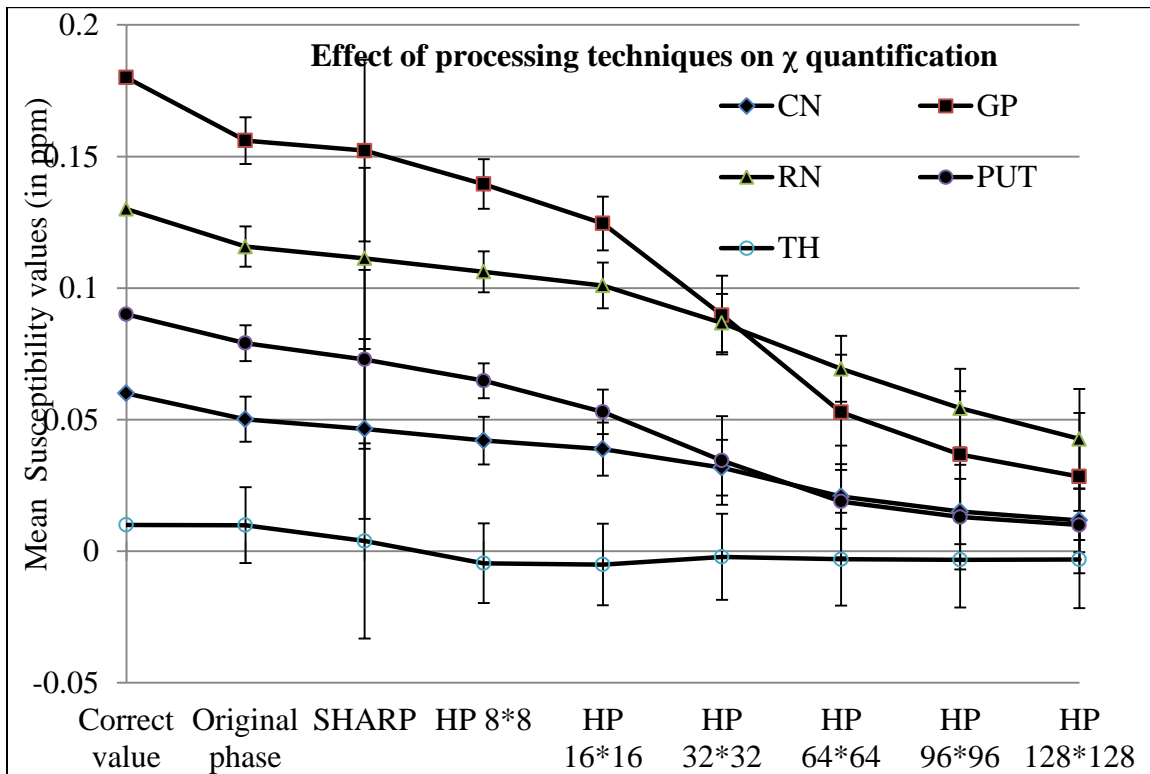


Figure 3.6: Relationship between the mean susceptibility value inside a given structure and the processing filters used on the original phase images produced from the brain model. CN=Caudate nucleus, GP=Globus pallidus, RN=Red nucleus, PUT=Putamen,

and TH=Thalamus. Imaging parameters: $B_0=3\text{Tesla}$, Echo time=18ms, pixel resolution= $0.5\times 0.5\times 0.5\text{mm}$ and regularization threshold of inverse filter=0.1.

The decrease in the mean susceptibility value seen in the susceptibility maps, inside the geometries after using various HP filter sizes and SHARP can be plotted and, later, can be used to extrapolate the true susceptibility values for the structures.

We will also discuss, in a later section of this chapter, the effect of HP filtering on creating the 'dark/bright bands' that are seen around large structures such as putamen and globus pallidus in Homodyne HP filtered SWI phase images and in their corresponding susceptibility maps.

3.3.1b) Inverse process:

Susceptibility mapping using phase information from the MRI signal has been immensely useful in elucidating the magnetic properties of different tissues. The methods to produce susceptibility maps from phase images usually use a regularized inverse approach [13], as explained in the previous chapter.

The brain model proposed is used to study the changes that are seen from the inverse process. This is done using both filtered and unfiltered phase with imaging parameters $B_0=3\text{T}$, $\text{TE}=18\text{ms}$ and pixel resolution= $(0.5\text{mm})^3$. *Figure 3.7* clearly demonstrates the streaking artifacts coming from the veins and from the basal ganglia structures with high susceptibility differences with respect to the white matter. Due to the loss of data in the

singularity region of k-space, an error is introduced in the susceptibility values inside the structure, as seen in the *Figure 3.6*. In subsection 3.3.2d) of this chapter, an ‘optimal echo time (TE)’ for susceptibility quantification is proposed.

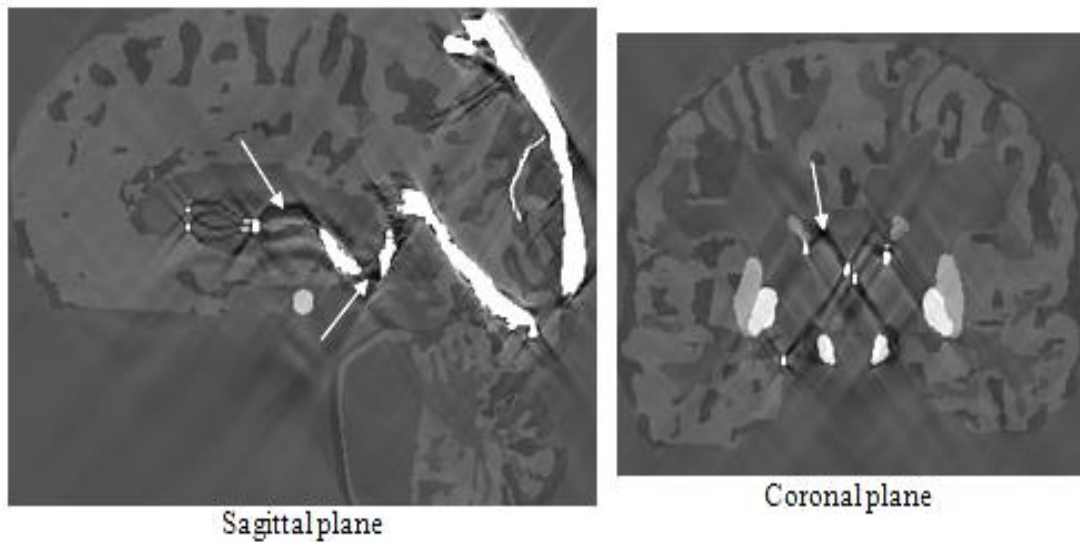


Figure 3.7: *Susceptibility maps generated from unfiltered simulated phase images (imaging parameters: $B_0=3T$, $TE=18\text{msec}$). Sagittal plane and coronal plane images shows the streaking artifacts (identified by the white arrows) introduced by the singularity problem in k-space in the inverse process.*

3.3.1c) Iterative algorithm:

The ill-posedness of the regularized inverse filter in generating the susceptibility maps can lead to severe streaking artifacts in susceptibility maps (Please refer to *Chapter 2.9*) as seen in *Figure 3.7* [30]. The iterative technique is used to try and remove these streaking artifacts. [30].

The initial susceptibility map is used to threshold the structure(s) of interest. The binary mask extracts the reconstructed susceptibility distribution inside the structure from the initial susceptibility map. The streaking artifacts associated with the structure are usually outside the structure; with less artifacts in the extracted susceptibility map. The k-space (generated using Fourier Transformation) of the extracted susceptibility map is used to replace the singularity region in the k-space of the initial susceptibility map. This replacement will provide realistic data points in the singularity region and reconstruction of this new k-space using Inverse Fourier transformation will produce a new susceptibility map with significantly reduced streaking artifacts. This procedure is repeated, by considering the new susceptibility map as the initial susceptibility map, until the error in the susceptibility value of the structure of interest between two consecutive iterations converges.

Figure 3.8 c) and 3.8e) demonstrates the reduction in streaking artifacts around the vessels. The iterative method can be used to remove streaking artifacts associated with not only vessels but also other brain structures by selecting the binary masks of different regions of interest, including the basal ganglia structures. This method is thoroughly explained and analyzed in the paper [30].

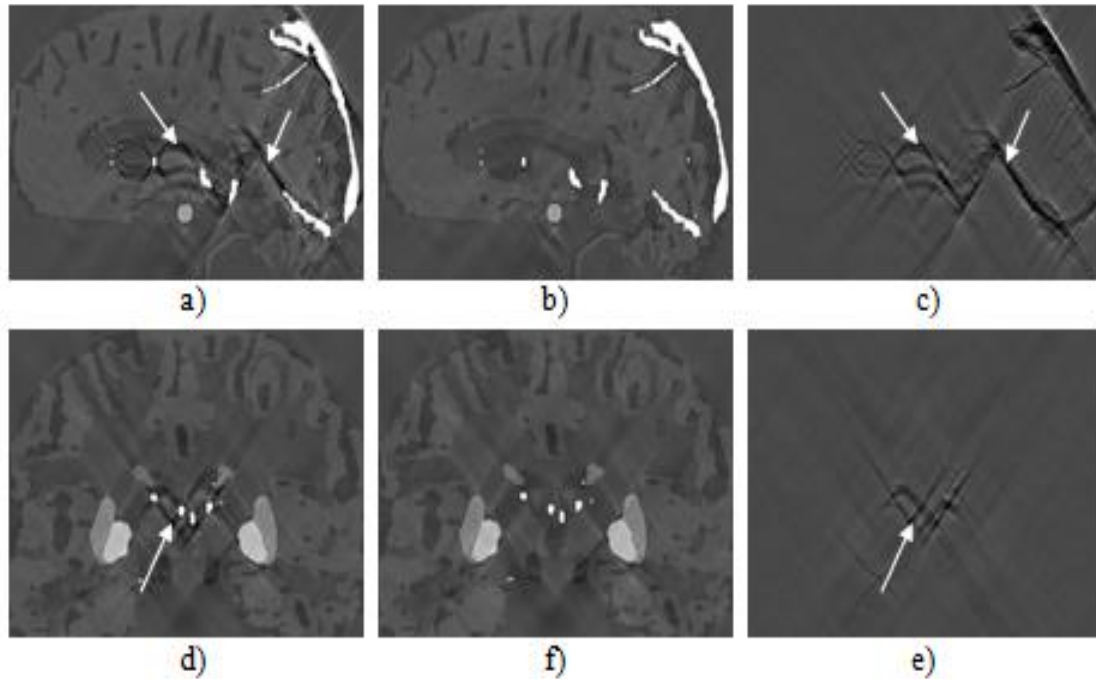


Figure 3.8: *Susceptibility maps before and after the iterative method using a binary mask which consists of vessels. a) Original susceptibility map without any noise added to the original simulated images (imaging parameters $TE=18ms$ and $B0=3T$) in sagittal view, b) Iterative result of a) after three iterations, c) The difference map of a) and b), d) Same original susceptibility map as a) in coronal view, e) Iterative result of a) after three iterations in coronal view, f) The difference map of d) and e). White arrows indicate the streaking artifacts seen in the original susceptibility maps a) and d). The difference maps show that this streaking noise is almost completely removed after three iterations of iterative method.*

3.3.2 Comparisons with In Vivo Human Phase Data

The phase simulations of the brain model can be compared with the *in vivo* human phase images by introducing confounding factors, such as partial volume effects (due to discretization of the MR signal) and white Gaussian noise (incorporated through real and imaginary channels).

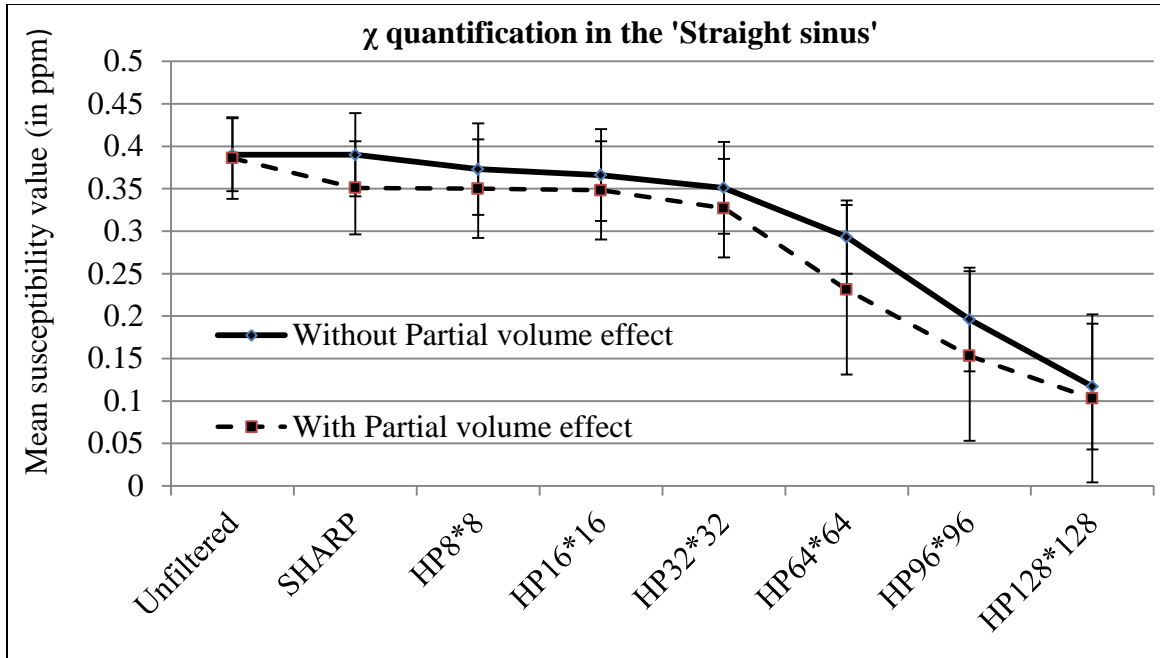
3.3.2a) Partial volume effects:

For a multi voxel sized objects, the voxel signal comes from a homogeneous tissue. On the other hand, for an object smaller than the voxel size, the signal will be integrated across the voxel; hence, causing it to be ‘partial volumed’ with the surrounding tissue. In phase images, the phase distribution across the voxel depends on the aspect ratio (x: y: z, where x, y and z are the dimensions of the voxel in x, y and z directions) and the resolution of the voxel. Low resolution causes a loss of phase information at the edges of the structures especially small blood vessels where the phase outside the boundary of the vessel decays by a factor of $1/r^2$ where r is the radius of the vessel [31]. Acquiring data with high pixel resolution helps in retaining the phase information and reducing these partial volume effects [32].

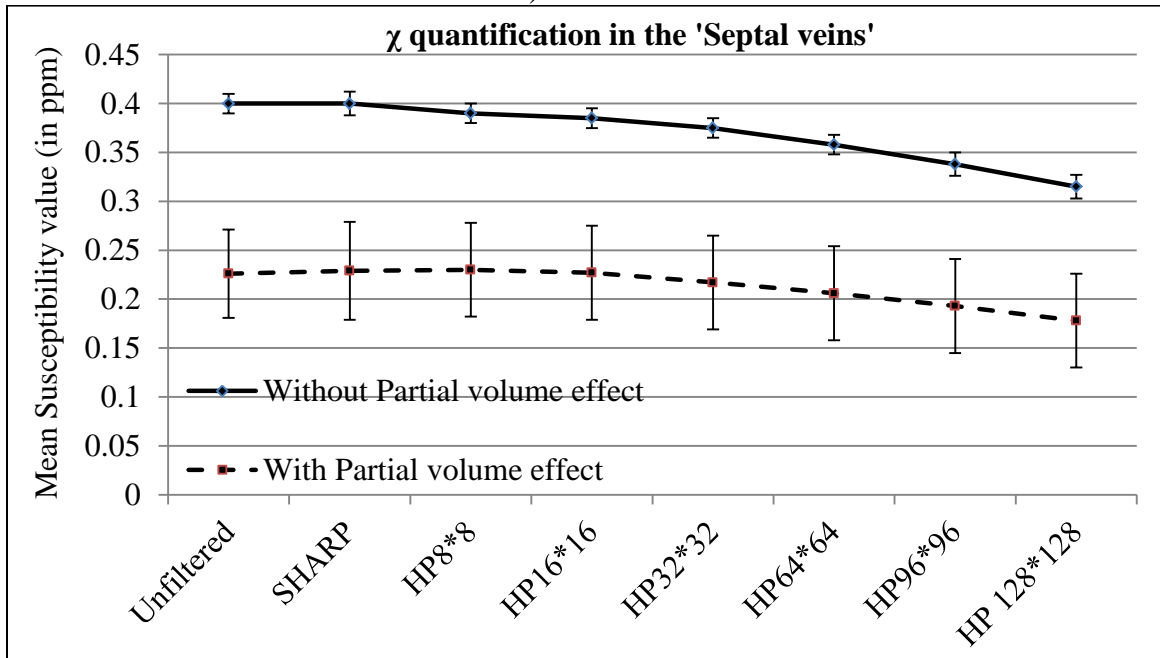
In order to simulate the effect of such an error, we performed a process analogous to the MRI image acquisition [28]. We start by simulating complex data, generated from the simulated phase images and magnitude images, with a pixel resolution of 125 microns (or micrometer), using a matrix size of 2048×2048×2048 pixels.

The simulation of the magnitude images using T_1 , T_2^* and spin density properties for different tissues is covered in *Chapter 4*. Then, a lower resolution images are obtained by taking the central part of its Fourier transform and applying an inverse Fourier transform to this cropped k-space matrix. The size of this cropped matrix is $512 \times 512 \times 512$ pixels, giving us the resolution of $(0.5\text{mm})^3$. This new data comprises of experimental artifacts such as Gibbs ringing and partial volume effects, making the phase behavior much more realistic. *Figure 3.9* shows the change in susceptibility value due to the partial volume effect. The diameter of a septal vein is much smaller than the straight sinus. Hence, the phase integration due to partial voluming clearly affects the reconstruction of septal vein more than the straight sinus in susceptibility mapping. The superior sagittal sinus is larger than the straight sinus, but it is not selected for the measurements to avoid any errors caused by the forward field calculations due its location at the edge of the brain.

The remaining part of this chapter will utilize this new phase data with partial volume effect, and will be referred to as the ‘simulated’ phase images. The comparison of the simulated phase maps and a real data set is done by matching the imaging parameters and the pixel resolution of the real data for the generation of simulated phase images.



a)



b)

Figure 3.9: Mean susceptibility value measurements of the straight sinus a) and septal veins b), from the susceptibility maps, generated from filtered and unfiltered phase, before and after simulating the partial volume effects (mimicking the discrete sampling of the MR signal). The susceptibility value of the septal vein is more affected by the partial

volume effect. The resolution of the image is $0.5 \times 0.5 \times 0.5 \text{mm}^3$ with aspect ratio of 1:1:1. The diameter of the straight sinus is around 8 pixels (4mm) and the diameter of the septal vein is 2 pixels (1mm) wide in the original model. The initial susceptibility value inside the veins was set to, $\Delta\chi=0.45\text{ppm}$. The partial voluming of the phase behavior around a small vessel like the septal vein severely affects the results of its reconstructed susceptibility distribution.

White Gaussian noise that is seen in the real images is added to the simulated images. MRI scanners generally introduce the noise while the signal is received through the real and imaginary channels [31]. Complex data that is produced from simulated phase images and magnitude images is used to generate simulated real and imaginary signals. Noise is added to these channels with a Signal-to-Noise Ratio (SNR) of 10:1. This ratio was calculated from the magnitude images of a real data from a homogeneous white matter region. Using the same image parameters as a given real data ($B_0=3\text{Tesla}$, $TE=18\text{msecs}$ and resolution $0.5 \times 0.5 \times 0.5 \text{mm}^3$), we can see in *Figure 3.10* that the simulations show very good agreement with the phase behavior seen in the real data.

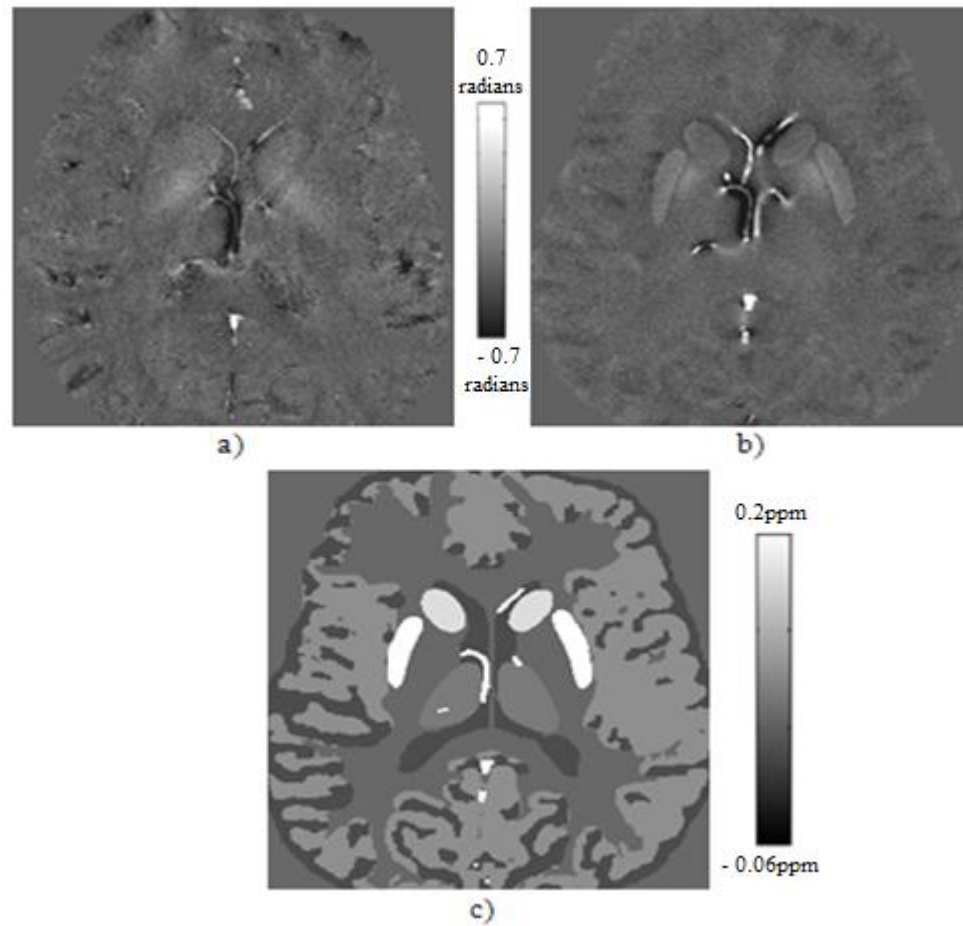


Figure 3.10: Comparison of a real phase data with the simulated phase with the same parameters as the real data. a) A real phase image, (Wayne State Research Facility) acquired using 3D GRE flow compensated-high resolution-SWI sequence, which is processed using SHARP (Sophisticated Harmonic Artifact Reduction on Phase data) method with imaging parameters $B_0=3T$ and $TE=18ms$. The imaging parameters and processing techniques are kept consistent in the simulated phase image b), c) A transverse view of the 3D brain model. Images a) and b) have the same window level settings.

3.3.2b) Red nucleus ‘halo’ effect:

‘Halo’ effect that is normally seen around the red nucleus in the real data has been believed to be representative of a capsule made up of dense medullated fibers around the boundary of the red nucleus [31, 33, 34]. For studies done in the past, this capsule has been known to generate contrast between the red nucleus and surrounding white matter in the SWI-Homodyne HP filtered phase images [35]. The real phase data filtered using the Homodyne HP filter and SHARP techniques are compared with the simulated phase images with the same imaging parameters, resolution and processing techniques (*Figure 3.11a*)).

This contrast is also seen outside the red nucleus in the simulated filtered phase images (*Figure 3.11b*) and *3.11d*)). In the brain model, there is no capsule surrounding the red nucleus. The ‘halo’ ring seen in simulated phase indicates that this effect might not be due to structural presence of a capsule around the red nucleus but it might be just an artifact caused by the phase behavior outside the red nucleus. Similar results were shown in [36] regarding the red nucleus ring by developing a model of red nucleus and substantia nigra. The proposed brain model in this thesis provides overall more accurate filtered-phase results since it includes the susceptibility distribution of the background tissues (grey and white matter with CSF), veins and other basal ganglia nuclei with homogeneous boundaries, which was not the case in the previous study.

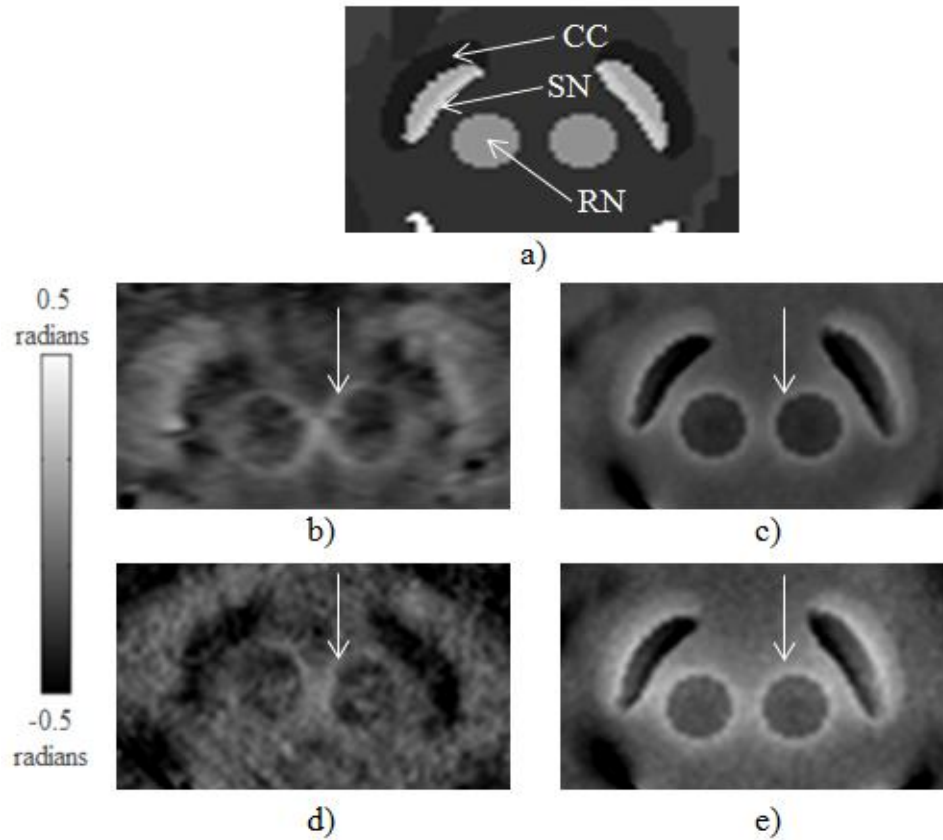


Figure 3.11: Comparison of the real phase information with simulated model phase profile of the rostral mid-brain area. a) Rostral mid-brain area in the brain model for reference, b) Homodyne HP-filtered real phase image ($TE=20\text{msec}$, $3T$, $0.5*0.5*2\text{mm}$ resolution, filter size $64*64$ pixels), c) Homodyne HP-filtered simulated phase data (same parameters and resolution as (b)), d) SHARP processed real phase data ($TE=18\text{msec}$, $3T$, $(0.5\text{mm})^3$) e) SHARP processed simulated phase data (same parameters as (d)). RN=Red Nucleus, SN=Substantia Nigra, CC=Crus Cerebri. The white arrows indicate the halo ring at the boundary of red nucleus in real and simulated phase data.

3.3.2c) False Internal Capsule:

Simulated susceptibility maps, after using HP filter, showed a negative susceptibility region outside structures. This dark region, which resembles the internal capsule, actually has a susceptibility difference ($\Delta\chi$) of 0ppm in the model (*Figure 3.4*). With the increase in the size of HP filter, this dark region changes in its extent and intensity (*Figure 3.13a*). These results are compared with the real data which show a similar dark region around basal ganglia after using HP filter (*Figure 3.12*). Susceptibility maps from the pure phase images show a marginal area with negative susceptibility in the internal capsule region (*Figure 3.12c*). Iterative algorithm is used on the susceptibility maps with different HP filter sizes; and without applying HP filter. The mean of the susceptibilities around the “internal capsule region” changes with different filter types (*Figure 3.13b*).

The error reduces as we increase the Homodyne HP filter size since these calculations are done over Internal Capsule region, so as we increase the homodyne HP filter size, there is a sharper dark region but the extent of internal capsule region decreases. Hence, the ‘mean’ chi value reduces. For SHARP processed SM, structures tend to preserve the phase information showing better contrast, and the dark region is less intense (*Figure 3.12(d) and 3.13(a)*). The dark region in the susceptibility maps of the filtered phase images does not appear to be affected after the usage of the iterative algorithm as much as SHARP processed data (*Figure 3.12(e), 3.12(g)*).

Homodyne HP filter changes the phase around the geometries due to the high frequency component. This effect is carried forward in susceptibility maps showing dark band

around the boundaries. Iterative algorithm is used to reduce the streaking artifacts. But, it does not identify and remove effects induced by HP filter. Hence, in HP data, dark regions are still seen after using the iterative algorithm. For unfiltered data, there is no HP effect at the edges; the artifacts would be due to inverse function and Gibbs ringing [37].

The reason of the slight dark region still present in SHARP data, after iterative algorithm, is because it works on the principle of removing the harmonic information from the phase data makes it sensitive to edges. 3D model has sharp boundaries creating some Gibbs ringing effect. This effect might be enhanced after using SHARP, which appears as the dark region. Hence, the knowledge of the contribution of the processing techniques in changing the phase behavior around the structures causing aforementioned negative susceptibility regions can be crucial; especially in the studies like iron detection in the progression of multiple sclerosis where iron containing regions appear similar to these dark regions.

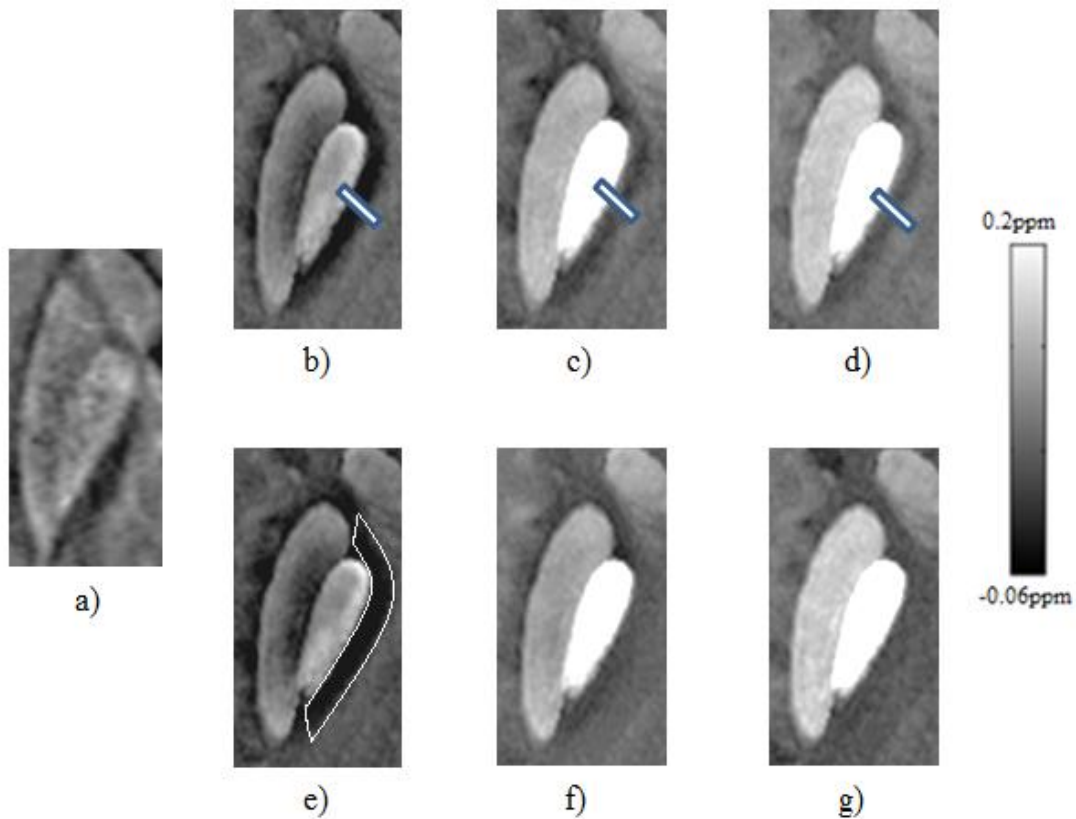
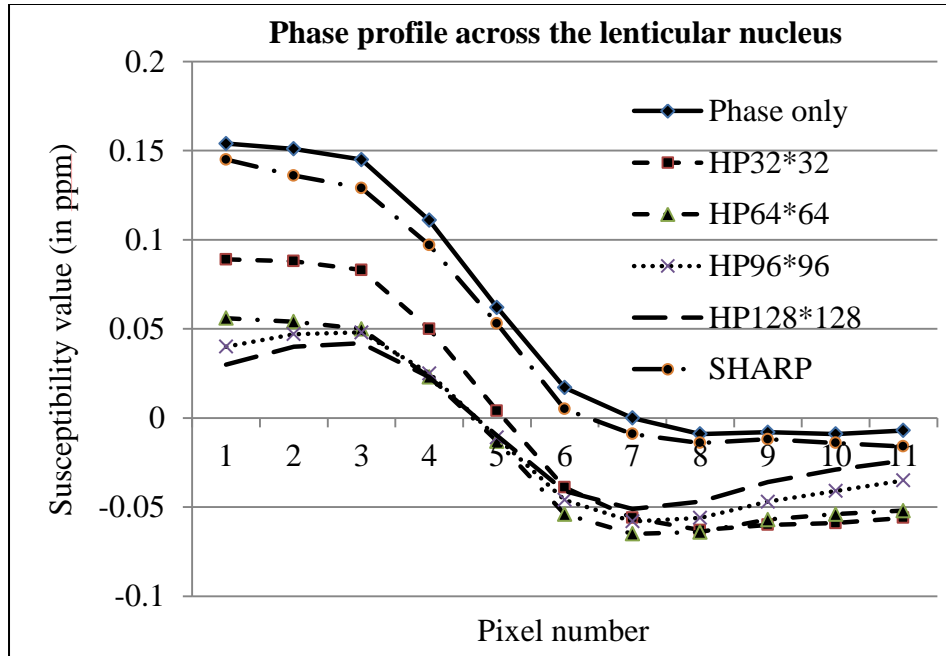
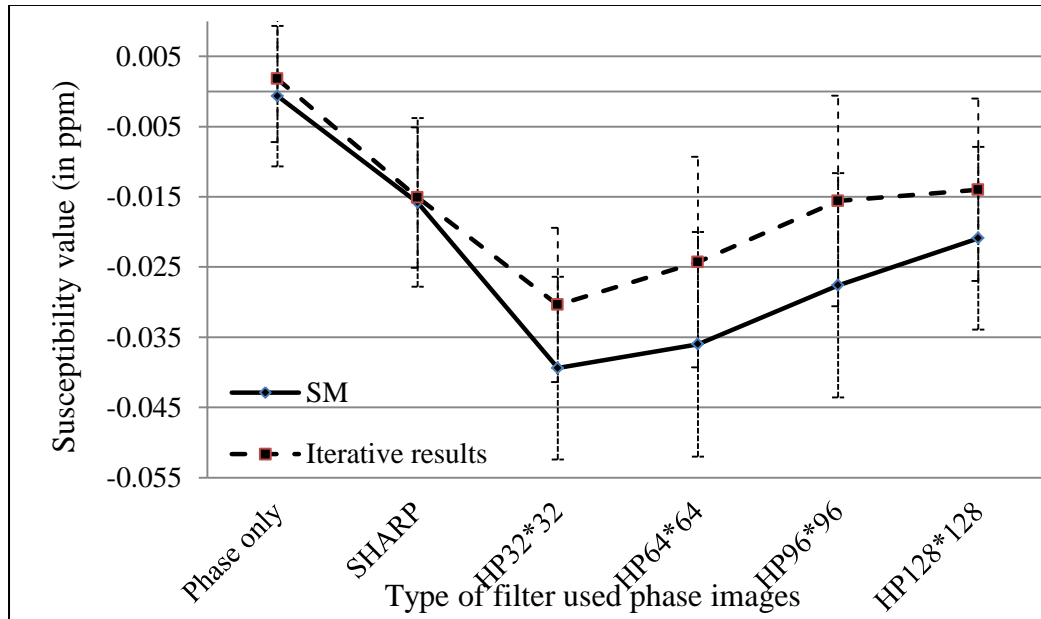


Figure 3.12: Comparison of susceptibility maps of the modeled data with various processing techniques and real data. Images show a part of basal ganglia surrounded by white matter, grey matter and CSF. Imaging parameters: $B_0=3T$, $TE=20\text{msecs}$ and resolution $0.5\times 0.5\times 2\text{mm}$. a) Susceptibility map of real data (HP filter size 64×64), b) Susceptibility map of modeled data (HP filter size 64×64), c) Susceptibility map of modeled data (unfiltered phase), d) Susceptibility map of SHARP processed phase, e), f) and g) are iterative results of (b), (c) and (d). The phase images for reconstructing the susceptibility maps shown in images b) – g) are generated using the same parameters and resolution as a).



a)



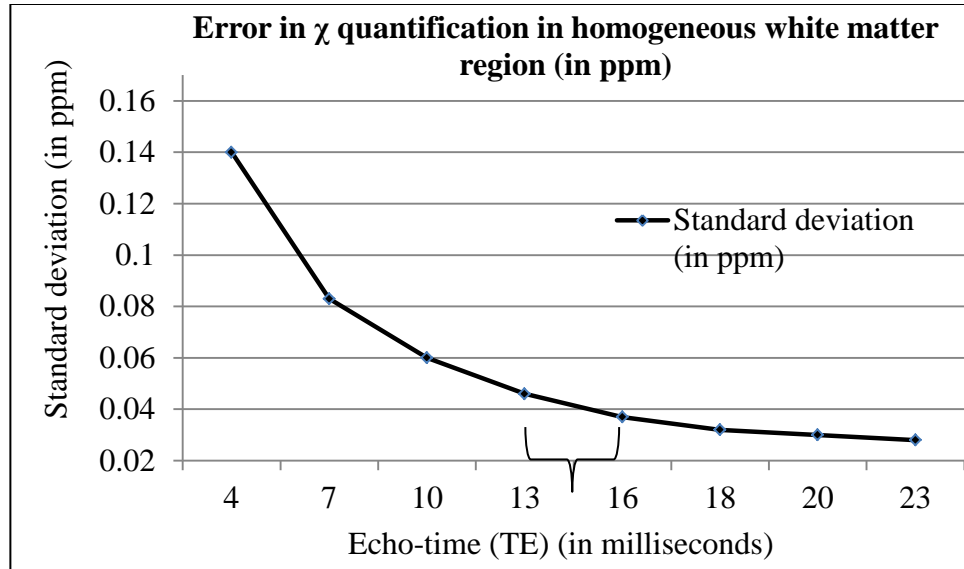
b)

Figure 3.13: a) Edge profile of susceptibility distribution from globus pallidus to the crus posterius [along the grey bar shown in Figure 3.12(b), (c), (d)]. b) Plot of mean susceptibility value over the internal capsule region (refer to the contour in Figure 3.12e)) at different HP filter sizes [actual $\Delta\chi_{(internal\ capsule)} = 0ppm$].

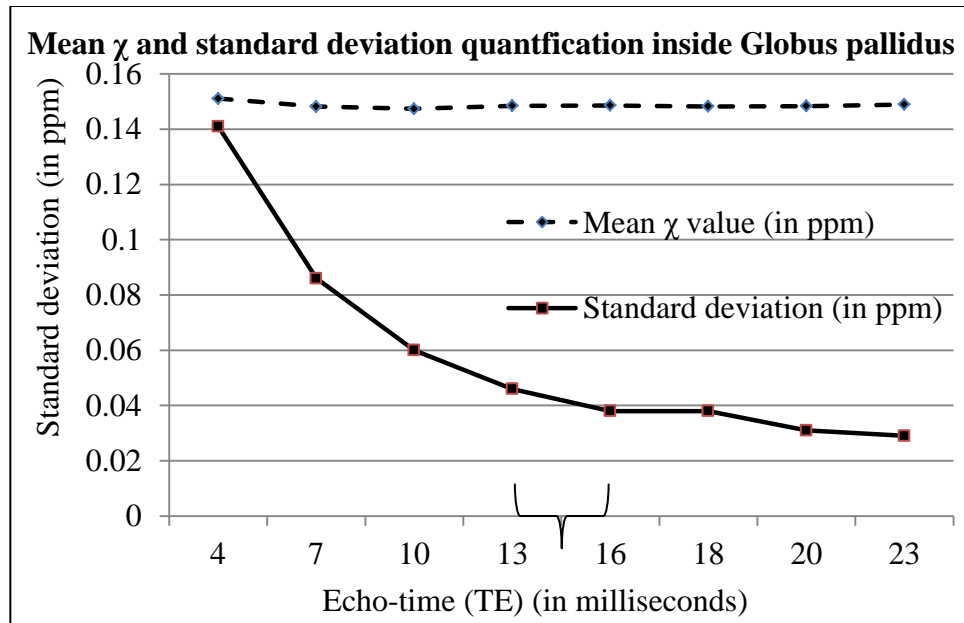
3.3.2d) Optimum Echo Time:

The brain model is used to determine the optimal echo time that produces lowest error in measuring susceptibility distribution. The model is used to simulated phase images at different echo times with a constant Signal to Noise ratio (SNR) of 10:1 in magnitude or 0.1 radians in phase images. To estimate the error, an area with homogeneous susceptibility is required. The region of white matter is selected on a 2D slice with no presence of any other structure, especially a vein, inside it in the three consecutive slices in the slice-select or z-direction.

As seen in *Figure 3.14*, the error in the susceptibility maps decreases as we increase the echo time. The reduction in this error seems significant between TE=4msec and TE=13msec. It should be noted that when the echo time equals the value of T_2^* relaxation of the structure it produces high signal and, thus, higher Signal-to-Noise Ratio (SNR) [31]. The standard deviation in phase images is equal to the inverse of SNR in magnitude images [31]. This may be the reason why we see the lowest standard deviation at around 20msec (T_2^* (globus pallidus) =19msec in the model) in *Figure 3.14b*). The susceptibility maps generated from echo times larger than 13ms (or 16ms) does not show much reduction in error. This shows that using echo time of 13ms will be a good practice since it makes the acquisition efficient by reducing the effective acquisition time.



a)



b)

Figure 3.14: Relationship between the echo time and the error in the susceptibility quantification in susceptibility maps. A constant white Gaussian noise (mean/standard deviation=10/1) was added to the real and imaginary components of the simulated data. a) The measurements are done in a homogeneous white matter region where the expected mean value is ideally zero, b) The measurements of mean χ value and the standard deviation are done inside the Globus pallidus ($\chi_{(globus\ pallidus)}=0.18\text{ppm}$).

Reference:

- [1] Haacke EM, Mittal S, Wue Z, Neelavalli J, Cheng YCN, “Susceptibility-Weighted Imaging: Technical Aspects and Clinical Applications, Part 1,” *American Journal of Neuroradiology*, vol. 30, 2009, pg.19-30.
- [2] Sokolowski J, Banks C, “*Principles of Modeling and Simulation: A Multidisciplinary Approach*,” Wiley and sons Inc., 2009.
- [3] Marques JP, Bowtell R. “Application of a Fourier-based method for rapid calculation of field inhomogeneity due to spatial variation of magnetic susceptibility,” *Concepts in Magnetic Resonance Part B: Magnetic Resonance Engineering*, vol. 25B, 2005, pg.65-78.
- [4] Salomir R, De Senneville BD, Moonen CTW, “A fast calculation method for magnetic field inhomogeneity due to an arbitrary distribution of bulk susceptibility,” *Concepts in Magnetic Resonance Part B: Magnetic Resonance Engineering*, vol. 19B, 2003, pg. 26-34
- [5] Hoffman RE, “Measurement of magnetic susceptibility and calculation of shape factor of NMR samples,” *Journal of Magnetic Resonance*, vol.178, 2006, pg.237-247.
- [6] Grahn JA, Parkinson JA, Owen AM, “The cognitive functions of the caudate nucleus,” *Progress in Neurobiology*, vol.86, 2008, pg.141-155.
- [7] Parent A, Carpenter M, “Human Neuroanatomy,” *Williams and Wilkins*, 9th edition, 1996.
- [8] Herrero MT, Barcia C, Navarro JM, “Functional anatomy of thalamus and basal ganglia,” *Child’s Nervous System*, vol. 18(8), 2002, pg.386–404.

- [9] DeArmond S, Fusco M, Dewey M, “*The Structure of the Human Brain: A Photographic Atlas,*” 2nd edition. New York: Oxford University Press, 1976. Copyright © 1976 by Oxford University Press, Inc.
- [10] Atasoy HT, Nuyan O, Tunc T, Yorubulut M, Unal AE, Inan LE, “T2-weighted MRI in Parkinson's disease; substantia nigra pars compacta hypointensity correlates with the clinical scores,” *Neurology India*, vol.52(3), 2004, pg.332-337.
- [11] Haacke EM, Makki M, Ge Y, Maheshwari M, Sehgal V, Hu J, Selvan M, Wu Z, Latif Z, Xuan Y, Khan O, Garbern J, Grossman RI, “Characterizing iron deposition in multiple sclerosis lesions using susceptibility weighted imaging,” *Journal of Magnetic Resonance Imaging*, vol. 29(3), 2009, pg. 537–544.
- [12] Swaiman KF, “Hallervorden-Spatz syndrome and brain iron metabolism,” *Archives of Neurology*, vol 48(12), 1991, pg.1285-1293.
- [13] Haacke EM, Tang J, Neelavalli J, Cheng YC, “Susceptibility Mapping as a Means to Visualize Veins and Quantify Oxygen Saturation,” *Journal of Magnetic Resonance Imaging*, 2010, vol. 32(3), pg.663-676.
- [14] Haacke EM, Cheng NY, House MJ, Liu Q, Neelavalli J, Ogg RJ, Khan A, Ayaz M, Kirsch W, Obenaus A, “Imaging iron stores in the brain using magnetic resonance imaging,” *Magnetic Resonance Imaging*, vol.23, 2005, pg.1–25.
- [15] Bydder GM, Young IR, “MR imaging: clinical use of the inversion recovery sequence,” *Journal of Computer Assisted Tomography*, vol. 9(4), pg.659–75.
- [16] Redpath T, Smith F, “Use of a double inversion recovery pulse sequence to image selectively grey or white brain matter,” *British Journal of Radiology*, vol.67, 1996, pg. 1258–1263.

- [17] Sezgin M, Bulent S, “Survey over image thresholding techniques and quantitative performance evaluation,” *Journal of Electronic Imaging*, vol. 13(1), 2004, pg.146-165.
- [18] Naidich T, Duvernoy H, Delman B, Sorensen A, Kollias S, Haacke M, “*Duvernoy's Atlas of the Human Brain Stem and Cerebellum*,” Springer, 1st edition, 2009.
- [19] Mugler J, Brookeman J, “Three-dimensional magnetization-prepared rapid gradient-echo imaging (3D MP RAGE),” *Magnetic Resonance in Medicine*, vol. 15(1), 1990, pg.152–157.
- [20] Bernstein M, King K, Zhou X, “*Handbook of MRI pulse sequences*,” Elsevier academic press, 2004.
- [21] Haacke EM, Xu Y, Cheng Y-CN, Reichenbach J, “Susceptibility weighted imaging (SWI),” *Magnetic Resonance in Medicine*, vol. 52, 2004, pg.612–618.
- [22] Spees WM, Yablonskiy DA, Oswald MC, Ackerman JJ, “Water proton MR properties of human blood at 1.5 Tesla: magnetic susceptibility, T(1), T(2), T*(2), and non-Lorentzian signal behavior,” *Magnetic Resonance in Medicine*, vol. 45, 2001, pg.533-542.
- [23] Qiu A, Brown T, Fischl B, Ma J, Miller MI, “Atlas Generation for Subcortical and Ventricular Structures with Its Applications in Shape Analysis,” *IEEE Trans Image Process*, vol. 19(6), 2010, 1539-47.
- [24] J. Talairach, P. Tournoux, “*Co-planar stereotaxic atlas of the human brain: 3-D Proportional System: An Approach to Cerebral Imaging*,” Thieme, 1988.

- [25] Collins D, Holmes C, Peters T, Evans A, “Automatic 3-D model-based neuroanatomical segmentation,” *Human Brain Mapping*, vol. 3(3), 1995, pg. 190-208.
- [26] Holmes CJ, Hoge R, Collins L, Woods R, Toga AW, Evans AC, “Enhancement of MR images using registration for signal averaging,” *Journal of Computer Assisted Tomography*, vol. 22(2), 1998, pg.324–333.
- [27] Wharton S, Bowtell R, “Whole-brain susceptibility mapping at high field: a comparison of multiple- and single-orientation methods,” *Neuroimage*, vol.53, 2010, pg.515-525.
- [28] Cheng YCN, Neelavalli J, Haacke EM, “Limitations of calculating field distributions and magnetic susceptibilities in MRI using a Fourier based method,” *Physics in Medicine and Biology*, vol. 54, 2009, pg.1169–1189.
- [29] Schweser F, Andreas D, Lehr BW, Reichenbach J, “Quantitative imaging of intrinsic magnetic tissue properties using MRI signal phase: an approach to in vivo brain iron metabolism?,” *NeuroImage*, vol.54 (4), 2011, pg.2789–2807.
- [30] Tang J, Liu S, Neelavalli, J, Buch S, Cheng, YC, Haacke EM, “Improving Susceptibility Mapping Using a Threshold-Based K-space/Image Domain Iterative Reconstruction Approach,” *Magnetic Resonance in Medicine*, 2012, Accepted for Publication.
- [31] Haacke EM, Brown R, Thompson M, Venkatesan R, “*Magnetic Resonance Imaging - Physical Principles and Sequence Design*,” *Wiley-Liss*, 1999.
- [32] Bruni J, Montemurro D, “*Human Neuroanatomy: A Text, Brain Atlas, and Laboratory Dissection Guide*,” *Oxford University Press*, 2009.

- [33] Barker LF, “*The nervous system and its constituent neurones: designed for the use of practitioners of medicine and of students of medicine and psychology,*” D.Appleton and Company, 1899.
- [34] Onodera S, Hicks P, Matsunami H, “A Comparative Neuroanatomical Study of the Red Nucleus of the Cat, Macaque and Human,” *Public Library of Science (PLoS) ONE*, vol. 4(8), 2009, e6623.
- [35] Manova ES, Habib CA, Boikov AS, Ayaz M, Khan A, Kirsch WM, Kido DK, Haacke EM, “Characterizing the mesencephalon using susceptibility-weighted imaging,” *American Journal of Neuroradiology*, vol.30(3), 2009, pg.569-74.
- [36] Schäfer A, Wharton S, Gowland P, Bowtell R, “Using magnetic field simulation to study susceptibility-related phase contrast in gradient echo MRI,” *Neuroimage*, vol.48, 2009, pg.126-137.
- [37] Bankman I, “*Handbook of medical imaging: processing and analysis,*” Academic press, 2000.

Chapter 4: T_2^* Mapping Using the Simulated Brain Model

The brain model is utilized to add tissue properties to each extracted structures and simulate MRI images pertaining to these tissue properties. In the previous chapter, modeling of MR phase data was explained by using tissue magnetic susceptibility properties. Similarly, this chapter covers the simulation of MRI magnitude data that is dependent on the T_1 , T_2 , T_2^* and spin density of the given tissue sample. *Chapter 2* focuses on the basics of MRI phase data and the content covered in this chapter extends these basic concepts by focusing on the magnitude component of an MR signal.

4.1 Basics of MRI Magnitude Signal:

In presence of an external magnetic field, the magnetization of a proton gets aligned in field direction. After application of a Radio Frequency (RF) field, which tips the magnetization away from the external magnetic field direction, the spin precesses back to the external field direction [1]. The precession of this spin and, hence, the changing magnetization of the spin produces current signal in the receiver coils of an MRI machine. The signal fades away as the spin aligns itself back towards the external magnetic field direction. This decay of the signal is caused due to two simultaneous processes, longitudinal or spin-lattice relaxation (T_1 relaxation) and transverse or spin-

spin relaxation (T_2 relaxation). These relaxation times are considered as tissue properties since they are different for different tissues [1].

4.1a) Spin density (ρ_0):

Spin density of a given sample can be described as the concentration of nuclei in tissue precessing at the Larmor frequency in a given region; and it is one of the principal determinants of the strength of the MR signals from that region [1].

4.1b) T_1 -Relaxation:

When the external magnetic field is applied along the z-axis at equilibrium condition, the net magnetization vector lies along the direction of the field M_z , known as the longitudinal magnetization, and it equals to the equilibrium magnetization M_0 . The x-axis and y-axis components of the magnetization are zero. When a required amount of energy is provided by applying an RF pulse in the transverse direction, the net magnetization is tipped away from the z-axis [2]. Due to the presence of the external magnetic field, the magnetization tends to return to its equilibrium state M_0 . With the help of thermal interactions between the precessing spins and the surrounding environment or ‘lattice’ the energy gained by the spins during RF excitation is dispersed to other nuclei in the lattice to gradually regain the longitudinal magnetization [1, 2]. The process of returning to equilibrium position is governed by a time constant T_1 :

$$M_z(t) = M_0 (1 - e^{-t/T_1}) \quad (4.1)$$

where, t = elapsed time, and considering that only transverse magnetization is present initially (i.e. $M_z(0)=0$). As shown in the *Figure 4.1a*), the equilibrium state is reached exponentially depending on the relaxation time T_1 .

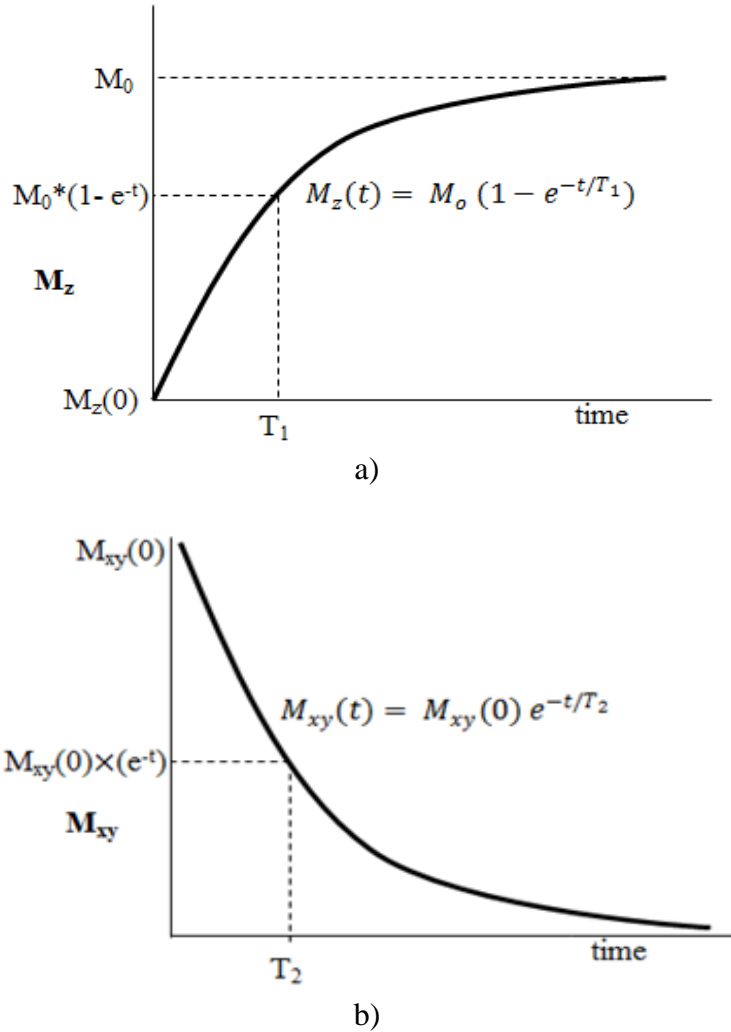


Figure 4.1: a) Recovery of the longitudinal component of the magnetization from initial value $M_z(0)$ to the equilibrium magnetization M_0 , b) The decay of the transverse magnetization from the initial value of $M_{xy}(0)$.

4.1c) T_2 -Relaxation:

In contrast to T_1 relaxation, the spin-spin relaxation is instrumental in the decay of transverse magnetization after the application of the RF pulse. The spin precessing towards the equilibrium magnetization experiences the combination of the external magnetic field and local fields from the neighboring spins [2]. The proton spins close to each other interact causing a phase shift between the spins ('dephasing') which reduces the net transverse magnetization vector (M_{xy}), the rate at which this happens depends on time constant T_2 [1].

$$M_{xy}(t) = M_{xy}(0) e^{-t/T_2} \quad (4.2)$$

Where, $M_{xy}(0)$ is the initial transverse magnetization, t =time elapsed. The time T_2 is shorter than T_1 , since the T_2 relaxation includes the dephasing effect and the spin-lattice couplings [1]. The relaxation times are also defined by their reciprocal forms:

$$R_1 = 1/T_2 \quad \text{and} \quad R_2 = 1/T_1 \quad (4.3)$$

Apart from the dephasing due to molecular interactions, the decay of transverse magnetization is affected the external magnetic field inhomogeneities causing an additional dephasing of the magnetization. This additional dephasing is denoted by another time constant T_2' [1]. Due to this the decay time of transverse magnetization is shortened and is given as T_2^*

$$1/T_2^* = 1/T_2 + 1/T_2' \quad \text{or} \quad R_2^* = R_2 + R_2' \quad (4.4)$$

In order to recover the loss of magnetization due to T_2' , an additional RF pulse (flip angle= 180°) can be incorporated in the MRI pulse sequence. This pulse will be used for rephasing of the spins, reversing the dephasing effect caused by the field inhomogeneities. The recovery of the initial phase relationship is produced in form of an 'echo', and decay of the transverse magnetization is characterized by the rate R_2 . This pulse sequence is known as Spin Echo sequence [1, 2]. For a Gradient Echo pulse sequence, there is no 180° pulse applied, hence the signal decays at the rate of R_2^* [1]. SWI pulse sequences are based on Gradient Echo sequences, hence, R_2^* or T_2^* effects are a very important factor for SWI magnitude images [3].

In addition to these macroscopic field inhomogeneities (macroscopic scale is more than a voxel size), there exists a microscopic intravoxel field inhomogeneity produced by the spatial variations of the magnetic susceptibilities within the region of interest [3]. These causes further dephasing and, hence, decay of the acquired signal [4,5].

4.2 T_2^* Mapping:

T_2^* relaxation time is related to the amount of iron deposited in the tissue, presence of iron in a tissue shortens the measured T_2^* relaxation of the tissue. Hence, T_2^* mapping (or $R_2^* = 1/T_2^*$, R_2^* is directly proportional to iron) is often utilized to assess the iron content in various tissue sites such as brain [6] and liver [7, 8]. T_2^* relaxation mapping has many other applications in MRI, including blood oxygenation level dependent (BOLD) functional imaging [6, 9,10], detection and tracking of super-paramagnetic iron oxides

(SPIO) [11]. The pathological tissues have different chemical composition (high content of water, demyelination, etc.) than the similar healthy tissues [12]. Qualitative and quantitative analysis of these decay rates can yield valuable information about the location and severity of the pathology. Accurate quantification of the T_2 and T_2^* may also allow to see the improvements of treatment for the disease [12].

The magnitude images, used for generating R_2^* maps, can be obtained from rapid acquisitions, such as RF (Radio Frequency) spoiled, short-TR (Repetition time), gradient-echo multi-echo sequences, which makes this technique particularly attractive for body imaging applications where motion is an important challenge [7]. The magnitude signal-intensity response for this RF-spoiled short-TR gradient-echo sequence is given by [1, 3]:

$$S = \rho_o \sin\theta \exp\left(-\frac{TE}{T_2^*}\right) \times \left[1 - \exp\left(-\frac{TR}{T_1}\right)\right] / \left[1 - \cos\theta \exp\left(-\frac{TR}{T_1}\right)\right] \quad (4.5)$$

where, TR is the Repetition time, TE represents the Echo time, and θ is the angle at which the longitudinal magnetization is tipped (flip angle) [1].

4.2a) Two-Echo Calculation

As mentioned above, once the protons in the tissue are excited, they tend to get back to the equilibrium low-energy state. The rate at which the magnetization and, hence, the signal decays (in case of pulse sequences such as Gradient Echo where the external magnetic in-homogeneities are not cancelled out) is given by the *Equation 4.5*.

For a multi-echo acquisition, where the repetition time (TR) is kept constant, T_2^* mapping can be done by taking signals (S_1 and S_2) from two different echoes TE_1 and TE_2 :

$$S_1 = S_0 \left(1 - e^{-\frac{TR}{T_1}}\right) e^{-TE_1/T_2^*}$$

$$\text{And, } S_2 = S_0 \left(1 - e^{-\frac{TR}{T_1}}\right) e^{-TE_2/T_2^*} \quad (4.6)$$

The ratio of these two signals gives us,

$$\frac{S_1}{S_2} = e^{-TE_1/T_2^*} / e^{-TE_2/T_2^*} \quad (4.7)$$

Taking logarithm of the expression gives:

$$\ln\left(\frac{S_1}{S_2}\right) = (TE_2 - TE_1)/T_2^*$$

$$\text{Hence, } T_2^* = (TE_1 - TE_2) / \ln\left(\frac{S_1}{S_2}\right) \quad (4.8)$$

4.2b) Multi-Echo Calculation

Equation (4.8) is simple and only allows a solution when there are only two echoes available. If we have more echoes, we can get a better result. *Equation (4.8)* will have issues when the echoes are too close to one end of the time spectrum (too small or too large).

If we had images taken at more than one echo time, we can get a better estimate of T_2^* by plotting the natural logarithm of the signal [$\ln(S)$] with respect to the respective echo time (i.e. plot $\ln(s)$ on Y axis and TE on X axis).

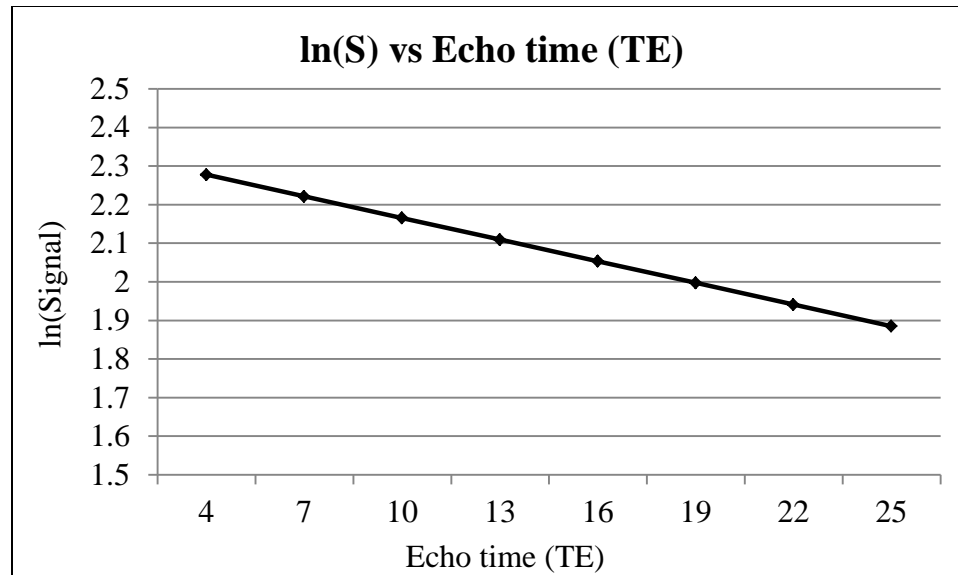


Figure 4.2: Relationship between the logarithm of the magnitude signal and the echo time (TE). A homogeneous white matter region signal from the simulated magnitude images (Figure 4.3) at different echo times (in msec: 4, 7, 10, 13, 16, 19, 22, 25) is used to plot this relationship.

4.2c) Non-linear Optimization

Another way to look at calculating the T_2^* , using a multiple echo data, is to plot the signal values as is (not take natural log) with respect to the echo times. Then compute the T_2^* using the non-linear best fit approach.

4.3 T_2^* Mapping Using the Brain Model:

The biological tissues have different values of the T_1 , T_2 and T_2^* relaxation rates. These tissue properties are added to the different structures in the model (Please refer to Figure 4.3) at a resolution of $0.5 \times 0.5 \times 0.5 \text{mm}^3$ in a matrix size of $512 \times 512 \times 512$. In the

previous chapter, the brain model was used to generate the susceptibility maps, by delineating susceptibility properties to different tissues that were utilized to make simulated phase images. Similarly, the T_1 , T_2^* and spin density values of the tissues are used to produce the simulated magnitude images using 4.5, where the flip angle= 15° is selected [1].

In order to compare these simulations with the real data, it is essential to simulate the partial voluming caused by the limited resolution in real life MRI acquisition due to the discretized sampling of the MR signal, as discussed in previous chapters [13]. Simulation of these effects in the phase images of the brain model by taking center of k-space data of the simulated phase image of very high matrix size, were discussed in *Chapter 3, subsection 3.3.2a*).

For the simulations, we have used a parabolic fitting method to estimate T_2^* maps from simulated magnitude images using 8 different echo times ($TE_1=4\text{ms}$, $TE_2=7\text{ms}$, $TE_3=10\text{ms}$, $TE_4=13\text{ms}$, $TE_5=16\text{ms}$, $TE_6=19\text{ms}$, $TE_7=22\text{ms}$, and $TE_8=25\text{ms}$) to estimate the T_2^* maps more accurately. The repetition time was decided as 35ms which is a reasonable approximation for an SWI acquisition at a resolution of $(0.5\text{mm})^3$.

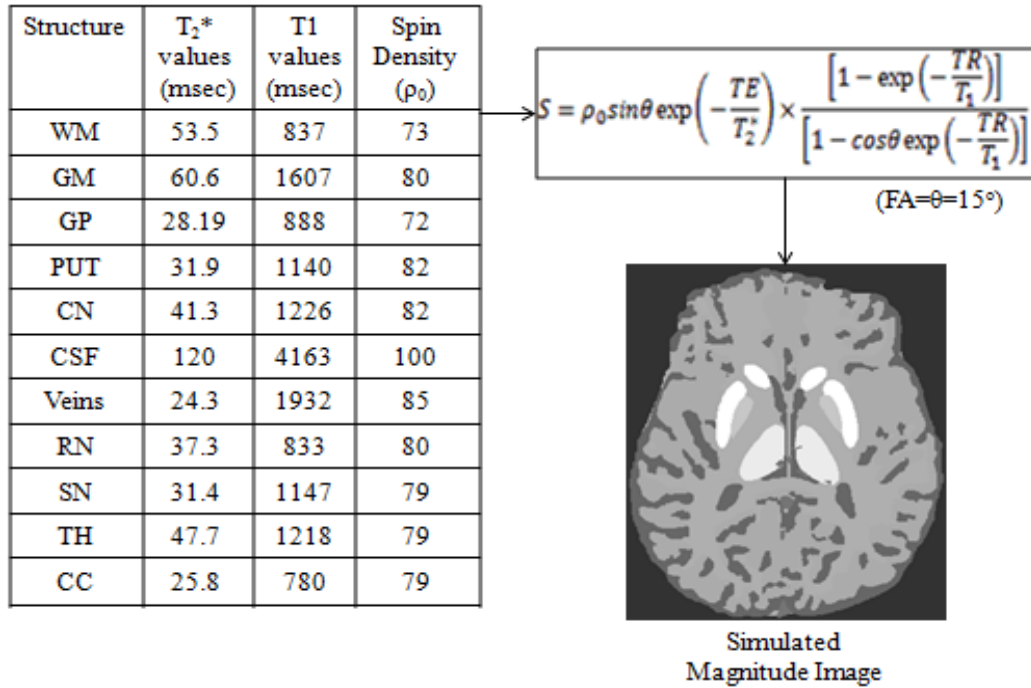


Figure 4.3: Spin density (ρ₀), T₁ and T₂* properties are added to each tissue in the brain model in order to generate magnitude images at main magnetic field, B₀, of 3Tesla for different echo times (T_n=4msec, 7msec, 10msec, 13msec, 16msec, 19msec, 22msec and 25msec) using 4.5 where flip angle of 15° is used. The reasonable values for ρ₀, T₁ and T₂* tissue properties are selected from real data processing (for spin density and T₂* values of basal ganglia structures) and literature [1, 14-21] at TR=35msec.

4.4 T₂* Error and Signal Loss:

Due to the macroscopic B₀ field inhomogeneities additional intravoxel dephasing is introduced in the acquired signal and results in faster signal decay. In conventional gradient echo imaging, susceptibility sensitivity is reflected as a T₂* signal loss in areas with field inhomogeneities [3, 5]. As explained earlier, the magnetic susceptibility of the tissue correlates with the magnetic response to the main magnetic field at microstructural

level [3]. Therefore, the intravoxel dephasing is caused by the presence of heterogeneous susceptibility distribution within a given tissue samples. The dephasing can lead to underestimation of T_2^* decay value (overestimation of R_2^*) [22] particularly at the edges of the tissues where there are high susceptibility changes [5].

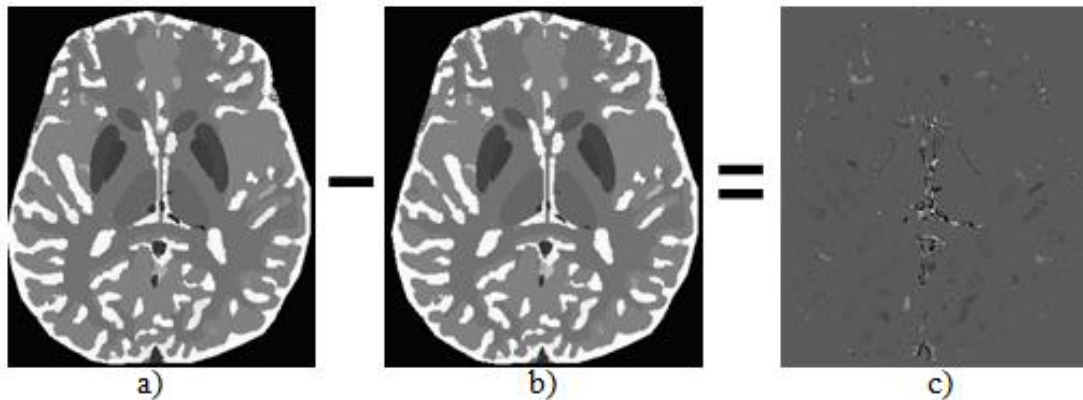


Figure 4.4: *a) T_2^* map generated by collapsing high resolution ‘complex’ data, b) T_2^* map generated by collapsing high resolution ‘magnitude’ data (no phase information), c) ‘ T_2^* residual error map’ or the difference image of b) subtracted from a) represents the change in T_2^* value which is caused by the signal loss due to local field variations in a).*

The magnitude images sometimes show areas with short T_2^* caused by the presence of deoxy-hemoglobin in the major veins [3]. This causes a much larger signal loss than the actual T_2^* of the tissue because the signal intensity from the vein can cancel the signal intensity from the grey matter or white matter. When the size of a vein is smaller than a voxel, it can cause a hypo-intense voxel with respect to its surroundings [3]. For larger veins, the partial volume voxels at the boundary of the vein is where the signal-intensity cancellations occur, producing hypo-intense voxels. This causes the vein to have a hypo-intense ring around its boundary (*Figure 4.5*). In order to estimate the error due to local

field variations, another complex data are simulated without any phase data. The magnitude images are collapsed from high resolution, same as mentioned above, without any phase information. The T_2^* maps calculated from both these data sets are subtracted to generate T_2^* residual error maps which will contain information about the change in T_2^* values only caused by the effects of tissue microstructure. The error maps generated by subtracting the estimated T_2^* maps and ideal T_2^* maps show that there a change in the T_2^* values at the region of heterogeneous susceptibility such the small vessels and edge of globus pallidus or substantia nigra (*Figure 4.6*).

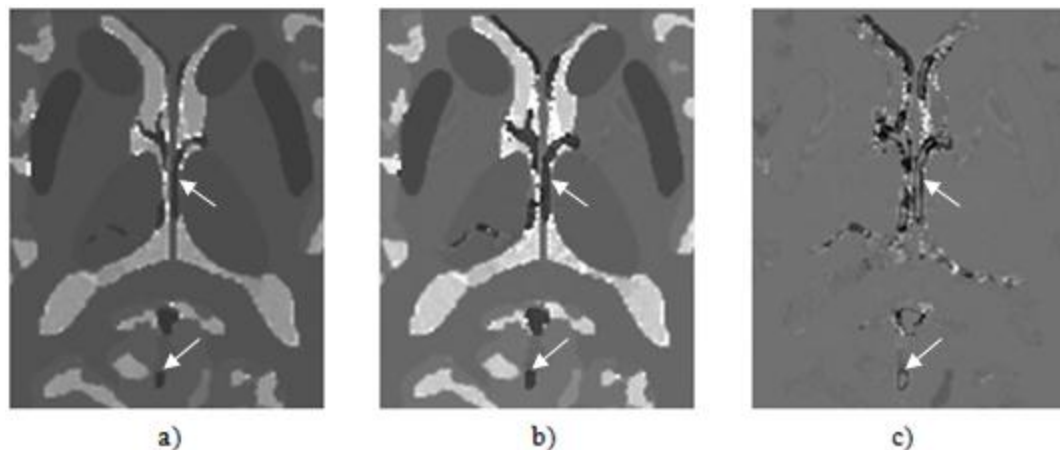


Figure 4.5: *a) Zoomed image (Fourier type zooming factor) of a T_2^* map generated by collapsing complex data, b) Zoomed image of a T_2^* map generated by collapsing magnitude (no phase information), c) T_2^* ‘residual error maps’ are produced by subtracting b) from a). The white arrows in the error map c) clearly shows the underestimation of the actual T_2^* values at the boundary of the vessels where there is relatively high susceptibility variations. a), b) and c) are at the same slice level.*

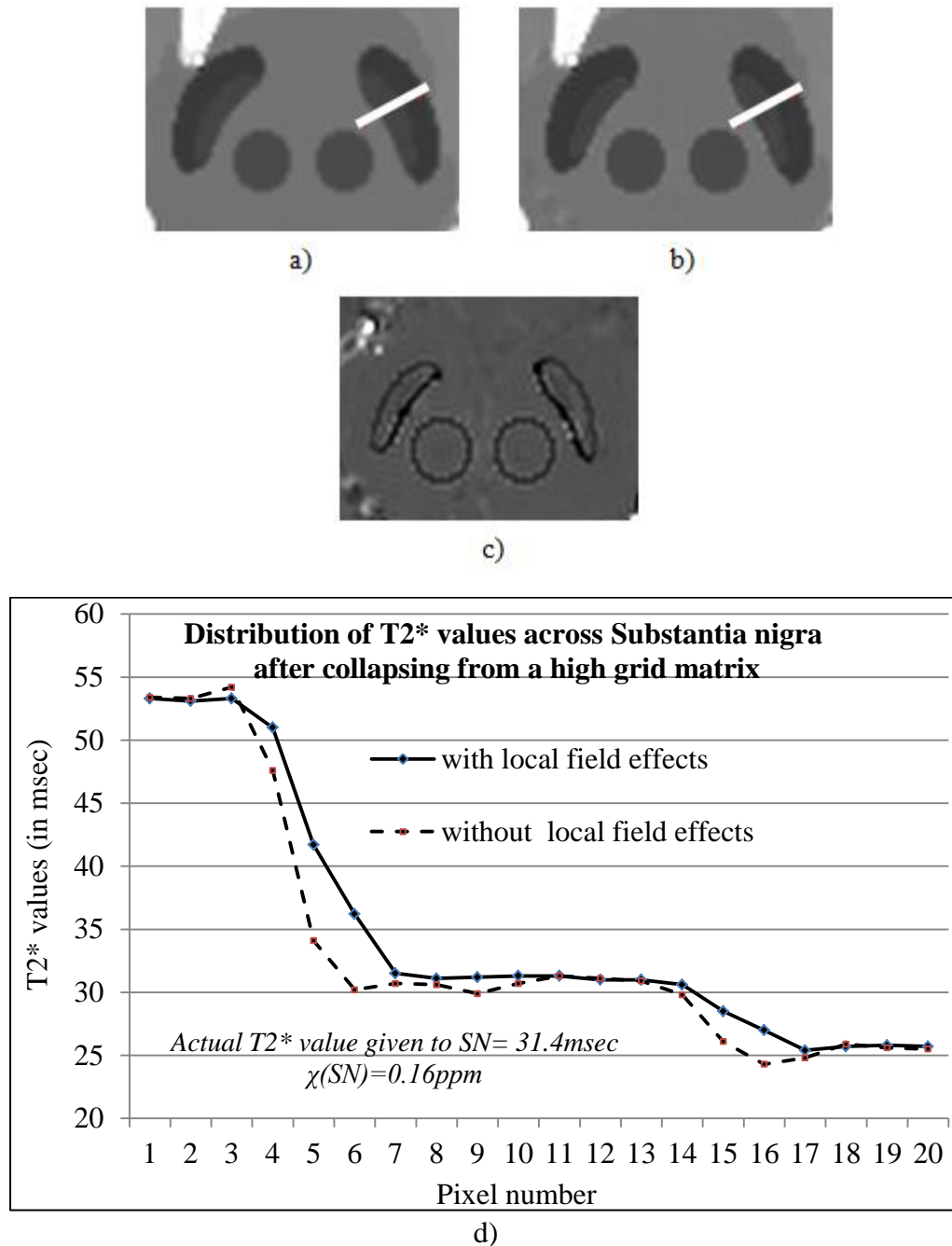


Figure 4.6: Comparison of the T_2^* maps, in rostral mid brain region, generated without a) and with b) local field variations due to susceptibility differences. T_2^* map of the latter case shows a reduction in T_2^* around the substantia nigra. c) The difference image of b) subtracted from a).

The comparison in *Figure 4.6* is shown between T_2^* distributions, in rostral mid brain area, generated from simulated magnitude data of the central k-space of the high resolution complex data with and without phase information. Many studies have shown that iron deposition in SN causes changes in dopaminergic pathways leading into Parkinson's disease [23-25]. High iron deposition in pars reticulata of the substantia nigra has been observed in cases with Hallervorden-Spartz syndrome [26]. *Figure 4.6d*) shows a T_2^* loss at the edge of the substantia nigra and a shift of approximately 3 pixels in the T_2^* behavior outside the boundary of the substantia nigra. Reduction in T_2^* correlates with iron, as mentioned earlier, but this T_2^* reduction at the boundary may be caused because of the signal loss due to the local field variations. Gibbs ringing is introduced at the edges after k-space cropping. The k-space collapsing of the complex data (with phase information) produces more amount of Gibbs ringing than the complex data without phase information. This is due to the presence of the additional local field variations in the region of heterogeneous susceptibility distribution. Hence, the residual T_2^* maps shows a small white ring which represents the difference in the amount of Gibbs ringing seen in T_2^* maps generated from the data with and without susceptibility induced phase information.

None of the effects of bulk field change from sinuses are introduced in the model and only the changes due to the local tissue microstructure are focused on. In conclusion, the error in T_2^* values is generated from the microscopic, intra-voxel, heterogeneous susceptibility distribution that local field variations as expected.

Reference:

- [1] Thompson M, Haacke EM, Brown R, Venkatesan R, “*Magnetic Resonance Imaging: Physical Principles and Sequence Design*, Wiley-Liss, 1999.
- [2] Bernstein M, King K, Zhou X, “*Handbook of MRI pulse sequences*,” Elsevier academic press, 2004.
- [3] Haacke EM, Mittal S, Wue Z, Neelavalli J, Cheng YCN, “Susceptibility-Weighted Imaging: Technical Aspects and Clinical Applications, Part 1,” *American Journal of Neuroradiology*, vol. 30, 2009, pg.19-30.
- [4] Haacke EM, Reichenbach J, “*Susceptibility Weighted Imaging in MRI: Basic Concepts and Clinical Applications*,” Wiley-Blackwell, 2011.
- [5] Hernando D, Vigen K, Shimakawa A, Reeder S, “ R_2^* Mapping in the Presence of Macroscopic B_0 Field Variations,” *Magnetic Resonance in Medicine*, Accepted 3 November, 2011.
- [6] Sadowski EA, Djamali A, Wentland AL, Muehrer R, Becker BN, Grist TM, Fain SB, “Blood oxygen level-dependent and perfusion magnetic resonance imaging: detecting differences in oxygen bioavailability and blood flow in transplanted kidneys,” *Magnetic Resonance Imaging*, vol. 28, 2010, pg.56–64.
- [7] Wood JC, Enriquez C, Ghugre N, Tyzka JM, Carson S, Nelson MD, Coates TD, “MRI R_2 and R_2^* mapping accurately estimates hepatic iron concentration in transfusion-dependent thalassemia and sickle cell disease patients,” *Blood*, vol. 106, 2005, pg.1460–1465.

- [8] Hankins JS, McCarville MB, Loeffler RB, Smeltzer MP, Onciu M, Hoffer FA, Li CS, Wang WC, Ware RE, Hillenbrand CM, “ R_2^* magnetic resonance imaging of the liver in patients with iron overload,” *Blood*, vol. 113, 2009, pg.4853–4855.
- [9] Ogawa S, Menon RS, Tank DW, Kim SG, Merkle H, Ellermann JM, Ugurbil K, “Functional brain mapping by blood oxygenation level-dependent contrast magnetic resonance imaging. A comparison of signal characteristics with a biophysical model,” *Biophysical Journal*, vol. 64, 1993, pg.803–812.
- [10] Beache GM, Herzka DA, Boxerman JL, Post WS, Gupta SN, Faranesh AZ, Solaiyappan M, Bottomley PA, Weiss JL, Shapiro EP, Hill MN, “Attenuated myocardial vasodilator response in patients with hypertensive hypertrophy revealed by oxygenation-dependent magnetic resonance imaging,” *Circulation*, vol.104, 2001, pg.1214–1217.
- [11] Dahnke H, Schaeffter T, “Limits of detection of SPIO at 3.0 T using T_2^* relaxometry,” *Magnetic Resonance in Medicine*, vol. 53, 2005, pg.1202–1206.
- [12] Tofts P, “*Quantitative MRI of the Brain: Measuring Changes Caused by Disease*,” Wiley, 2005.
- [13] Cheng YCN, Neelavalli J, Haacke EM, “Limitations of calculating field distributions and magnetic susceptibilities in MRI using a Fourier based method,” *Physics in Medicine and Biology*, vol. 54, 2009, pg.1169–1189.
- [14] Vymazal J, Righini A, Brooks RA, Canesi M, Mariani C, Leonardi M, Pezzoli G, “T1 and T2 in the brain of healthy subjects, patients with Parkinson disease, and patients with multiple system atrophy: relation to iron content,” *Radiology*, vol. 211(2), 1999, pg.489-495.

- [15] Lu H, Clingman C, Golay X, van Zijl PC, “Determining the longitudinal relaxation time (T1) of blood at 3.0 Tesla,” *Magnetic Resonance in Medicine*, vol 52(3), 2004, pg.679-682.
- [16] Yang Q, Liu J, Barnes SR, Wu Z, Li K, Neelavalli J, Hu J, Haacke EM, “Imaging the vessel wall in major peripheral arteries using susceptibility-weighted imaging,” *Journal of Magnetic Resonance Imaging*, vol. 30(2), 2009, pg.357-65.
- [17] Oros-Peusquens AM, Laurila M, Shah NJ, “Magnetic field dependence of the distribution of NMR relaxation times in the living human brain,” *Magnetic Resonance Materials in Physics, Biology and Medicine (MAGMA)*, vol. 21(1-2), 2008, pg.131-147.
- [18] Gelman N, Ewing JR, Gorell JM, Spickler EM, Solomon EG, “Interregional variation of longitudinal relaxation rates in human brain at 3.0 T: relation to estimated iron and water contents,” *Magnetic Resonance in Medicine*, vol 45(1), 2001, pg.71-79.
- [19] Wansapura JP, Holland SK, Dunn RS, Ball WS Jr, “NMR relaxation times in the human brain at 3.0 tesla,” *Journal of Magnetic Resonance Imaging*, vol. 9(4), 1999, pg.531-538.
- [20] Lin C, Bernstein M, Huston J, Fain S, “Measurements of T1 Relaxation times at 3.0T: Implications for clinical MR,” *Proceedings of the International Society for Magnetic Resonance in Medicine*, 9, 2001.
- [21] Péran P, Hagberg G, Luccichenti G, Cherubini A, Brainovich V, Celsis P, Caltagirone C, Sabatini U, “Voxel-based analysis of R2* maps in the healthy human brain,” *Journal of Magnetic Resonance Imaging*, vol. 26(6), 2007,pg.1413-1420.

- [22] Fernández-Seara MA, Wehrli FW, “Postprocessing technique to correct for background gradients in image-based R_2^* measurements,” *Magnetic Resonance in Medicine*, vol. 44, 2000, pg.358–366.
- [23] Yan SQ, Sun JZ, Yan YQ, Wang H, Lou M, “Evaluation of Brain Iron Content Based on Magnetic Resonance Imaging (MRI): Comparison among Phase Value, R_2^* and Magnitude Signal Intensity,” *PLoS ONE*, vol. 7, 2012, e31748.
- [24] Sofic E, Riederer P, Heinsen H, Beckmann H, Reynolds GP, Hebenstreit G, Youdim MBH, “Increased iron (III) and total iron content in post mortem substantia nigra of parkinsonian brain,” *Journal of Neural Transmission*, vol. 74, 1988, pg.199-205.
- [25] Dexter DT, Wells FR, Lees AJ, Agid F, Agid Y, Jenner P, Marsden CD, “Increased Nigral Iron Content and Alterations in Other Metal Ions Occurring in Brain in Parkinson's Disease,” *Journal of Neurochemistry*, vol. 52, 1989, pg.1830-1836.
- [26] Swaiman KF, “Hallervorden-Spatz syndrome and brain iron metabolism,” *Archives of Neurology*, vol 48(12), 1991, pg.1285-1293.

Chapter 5: Future Directions

The brain model currently includes the structures of basal ganglia, mid brain, grey matter, white matter, major veins and cerebrospinal distribution. The model has demonstrated that by adding required tissue properties, it can be used to generate simulated phase and magnitude images that may be used to predict and study the normal signal behavior.

Introduction of real life imperfections to these images has helped the results to be even more comparable with the real data.

In conclusion to the results shown in *Chapter 3*, the brain model demonstrates its role in studying the phase signal around different brain structures. The appearance of structures like capsule of red nucleus in the simulated filtered-phase images and the internal capsule region in susceptibility maps, both of which are not included in the model, presents a topic of discussion whether these signal are developed due to the processing techniques as artifacts or not. If not, then how much of this signal is introduced or exacerbated by the filtering of the original phase information. Adding these structures, such as the red nucleus capsule and internal capsule region, of the brain to this model will provide a better comprehensive result. The subsequent step should, therefore, be to add more tissue geometries such as brain stem structures, hippocampus, etc., to develop a complete brain model.

The goal of creating a high resolution 3D model of the human brain $(0.5\text{mm})^3$ was to generate a test phantom for susceptibility mapping that mimicked the usual resolutions collected in either research or clinical scanning. At this resolution, there is considerably less partial volume effect for most structures in the brain (except for very small vessels), which allows efficient reconstruction. The real phase data is mostly acquired at a resolution lower than $(0.5\text{mm})^3$ due to long acquisition time required for higher resolution although there are some new segmented echo planar sequences under development that could make 0.5mm^3 clinically viable [2].

The model can definitely be improved by using even higher resolution datasets to extract structures (for example, extracting veins from a high resolution $0.25 \times 0.25 \times 0.5\text{mm}^3$ contrast enhanced MRV dataset or by simply interpolating the structures in all three directions. This will be helpful to simulate very small blood vessels such as the medullary veins (diameter less than 250microns) originating from the septal veins. The real data acquired at 7T can be used for extraction of the structures due to the high SNR offered at such high field strength.

The results presented in this thesis pertain to the signal behavior from the local tissue geometries. Parallel to developing the whole brain model of the tissues, it is also essential to incorporate global geometries such as the air-tissue interfaces at the sinuses which are the source of unwanted global magnetic field perturbations, as mentioned in *Chapter 2*. The simulated T_2^* maps may be estimated in presence of these interfaces to understand in the detail the error introduced in the T_2^* values [1].

Testing the inverse process to generate susceptibility maps can also be done using a regularized kernel of the Green's function. There are other kernels that can be used for the inverse process and these kernels can be compared using the brain model introduced in this thesis as a means to identify the accuracy for each kernel in the inverse process [3]. Apart from the addition of healthy brain tissues, inclusion of abnormal tissues such as microbleeds and MS white matter lesions will help in analyzing more clinically relevant data.

Reference:

- [1] Hernando D, Vigen K, Shimakawa A, Reeder S, “ R_2^* Mapping in the Presence of Macroscopic B_0 Field Variations,” *Magnetic Resonance in Medicine*, Accepted 3 November, 2011.
- [2] Xu Y, Haacke EM, “An iterative reconstruction technique for geometric distortion-corrected segmented echo-planar imaging,” *Magnetic Resonance Imaging*, vol. 26(10), 2008, pg.1406-1414.
- [3] Jenkinson M, Wilson J, Jezzard P, “Perturbation Method for Magnetic Field Calculations of Nonconductive Objects,” *Magnetic Resonance in Medicine*, vol. 52, 2004, pg.471– 477.